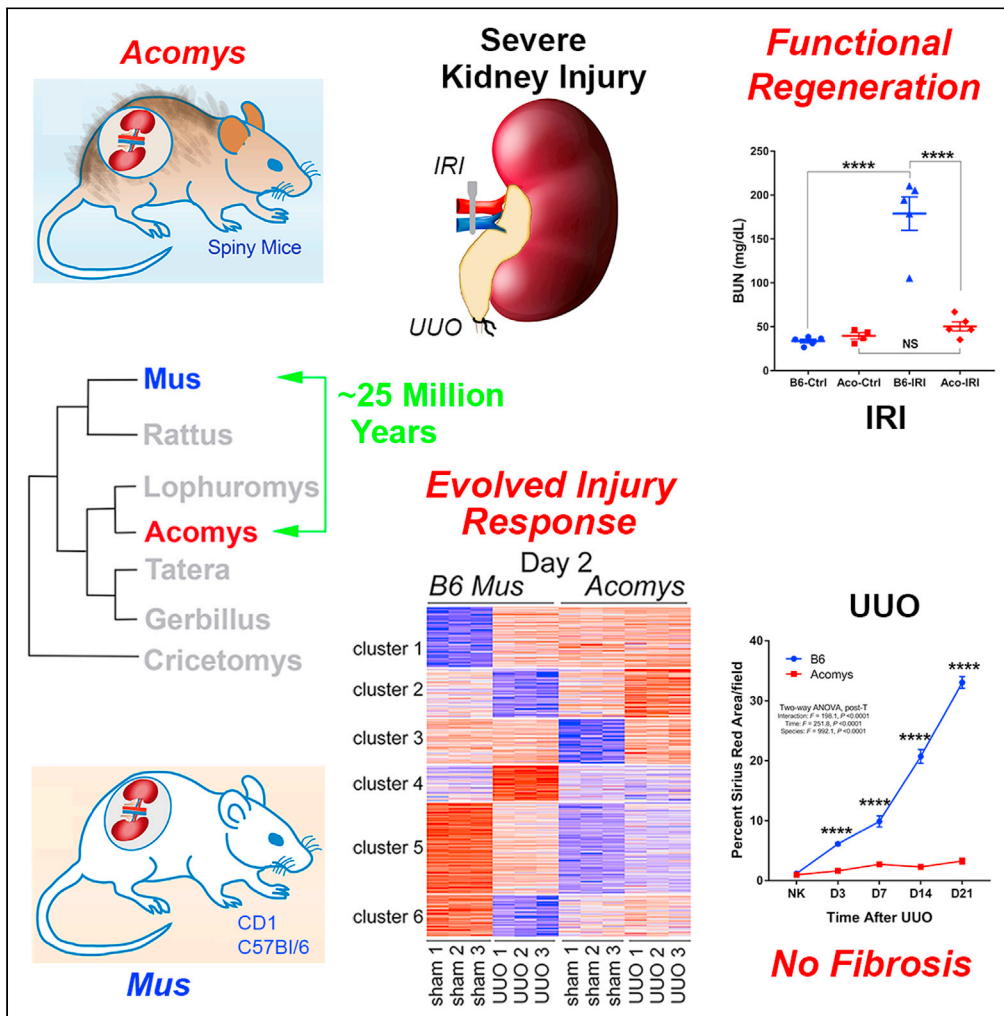


Article

Spiny mice activate unique transcriptional programs after severe kidney injury regenerating organ function without fibrosis



Daryl M. Okamura, Chris M. Brewer, Paul Wakenight, ..., Kathleen J. Millen, David R. Beier, Mark W. Majesky

daryl.okamura@seattlechildrens.org (D.M.O.)
mwm84@uw.edu (M.W.M.)

Highlights
Acomys fully regenerate kidney structure and function without fibrosis after injury

Unique gene clusters rapidly activated in surviving cells align with regeneration

Acomys genome appears poised at the time of kidney injury to initiate regeneration



Article

Spiny mice activate unique transcriptional programs after severe kidney injury regenerating organ function without fibrosis

Daryl M. Okamura,^{1,3,9,*} Chris M. Brewer,^{2,3,8,9} Paul Wakenight,⁴ Nadia Bahrami,³ Kristina Bernardi,³ Amy Tran,³ Jill Olson,³ Xiaogang Shi,³ Szu-Ying Yeh,⁴ Adrian Piliponsky,⁵ Sarah J. Collins,³ Elizabeth D. Nguyen,^{1,3} Andrew E. Timms,³ James W. MacDonald,⁶ Theo K. Bammler,⁶ Branden R. Nelson,⁴ Kathleen J. Millen,^{1,4} David R. Beier,^{1,3} and Mark W. Majesky^{1,2,3,7,10,*}

SUMMARY

Fibrosis-driven solid organ failure is an enormous burden on global health. Spiny mice (*Acomys*) are terrestrial mammals that can regenerate severe skin wounds without scars to avoid predation. Whether spiny mice also regenerate internal organ injuries is unknown. Here, we show that despite equivalent acute obstructive or ischemic kidney injury, spiny mice fully regenerate nephron structure and organ function without fibrosis, whereas C57Bl/6 or CD1 mice progress to complete organ failure with extensive renal fibrosis. Two mechanisms for vertebrate regeneration have been proposed that emphasize either extrinsic (pro-regenerative macrophages) or intrinsic (surviving cells of the organ itself) controls. Comparative transcriptome analysis revealed that the *Acomys* genome appears poised at the time of injury to initiate regeneration by surviving kidney cells, whereas macrophage accumulation was not detected until about day 7. Thus, we provide evidence for rapid activation of a gene expression signature for regenerative wound healing in the spiny mouse kidney.

INTRODUCTION

Solid organ failure is the result of dysregulated wound healing that leads to progressive loss of tissue function, fibrosis, and eventual organ failure (Duffield et al., 2013; Humphreys, 2018). The global health burden for loss of vital organ function due to progressive fibrosis is enormous (Gurtner et al., 2008). There are currently very few treatment options for patients with end-stage kidney disease or similar degenerative fibrotic conditions of the heart, lungs, liver, or reproductive organs (Hill et al., 2016; Rockey et al., 2015). Looking at nature for a possible solution, it was reported that adult rodents of the genus *Acomys* (spiny mice) can shed their dorsal skin as a deterrent to avoid predators and fully regenerate the lost tissue without fibrosis or tissue overgrowth (Seifert et al., 2012). The restored skin is complete with hair follicles, sebaceous glands, cartilage, adipose tissue, nerves, muscle, and blood vessels in the correct pattern and architectural organization (Seifert et al., 2012; Gawriluk et al., 2016; Matias Santos et al., 2016). Although this remarkable wound healing response in the skin has been examined in considerable detail (Brant et al., 2015; Gawriluk et al., 2016; Matias Santos et al., 2016; Simkin et al., 2017; Jiang et al., 2019), whether or not scarless regenerative wound healing in *Acomys* species extends beyond skin to vital internal organs remains unknown.

In the experiments reported here, our objective was to produce injuries to *Acomys* kidney that are known to promote severe fibrotic responses, leading to organ failure in *Mus musculus*. Our goal was to test whether or not regenerative wound healing observed in *Acomys* skin is also found for the injured adult kidney. We show that in two aggressive models of kidney disease, unilateral ureter obstruction (UUO) and ischemia reperfusion injury (IRI), there was a complete absence of fibrosis and rapid regeneration of kidney structure and nephron function in *Acomys*. By contrast, paired groups of *Mus* (outbred CD1 or inbred C57Bl/6J) developed severe kidney fibrosis that rapidly progressed to complete renal failure. Comparative transcriptomics showed the initiation of differential gene regulation in injured *Acomys* kidney, compared with *Mus*, was rapid (day 2) and preceded the accumulation of F4/80-positive macrophages (day 7). These

¹Department of Pediatrics, University of Washington, Seattle, WA 98195, USA

²Department of Laboratory Medicine & Pathology, University of Washington, Seattle, WA 98195, USA

³Center for Developmental Biology & Regenerative Medicine, Seattle Children's Research Institute, Seattle, WA 98105, USA

⁴Center for Integrated Brain Research, Seattle Children's Research Institute, Seattle, WA 98105, USA

⁵Center for Immunity & Immunotherapies, Seattle Children's Research Institute, Seattle, WA 98105, USA

⁶Department of Environmental & Occupational Health, University of Washington, Seattle, WA 98195, USA

⁷Institute of Stem Cell & Regenerative Medicine, University of Washington, Seattle, WA 98195, USA

⁸Present address: Lightspeed Microscopy, Inc., Seattle, WA, USA

⁹These authors contributed equally

¹⁰Lead contact

*Correspondence: daryl.okamura@seattlechildrens.org (D.M.O.), mwm84@uw.edu (M.W.M.)
<https://doi.org/10.1016/j.isci.2021.103269>



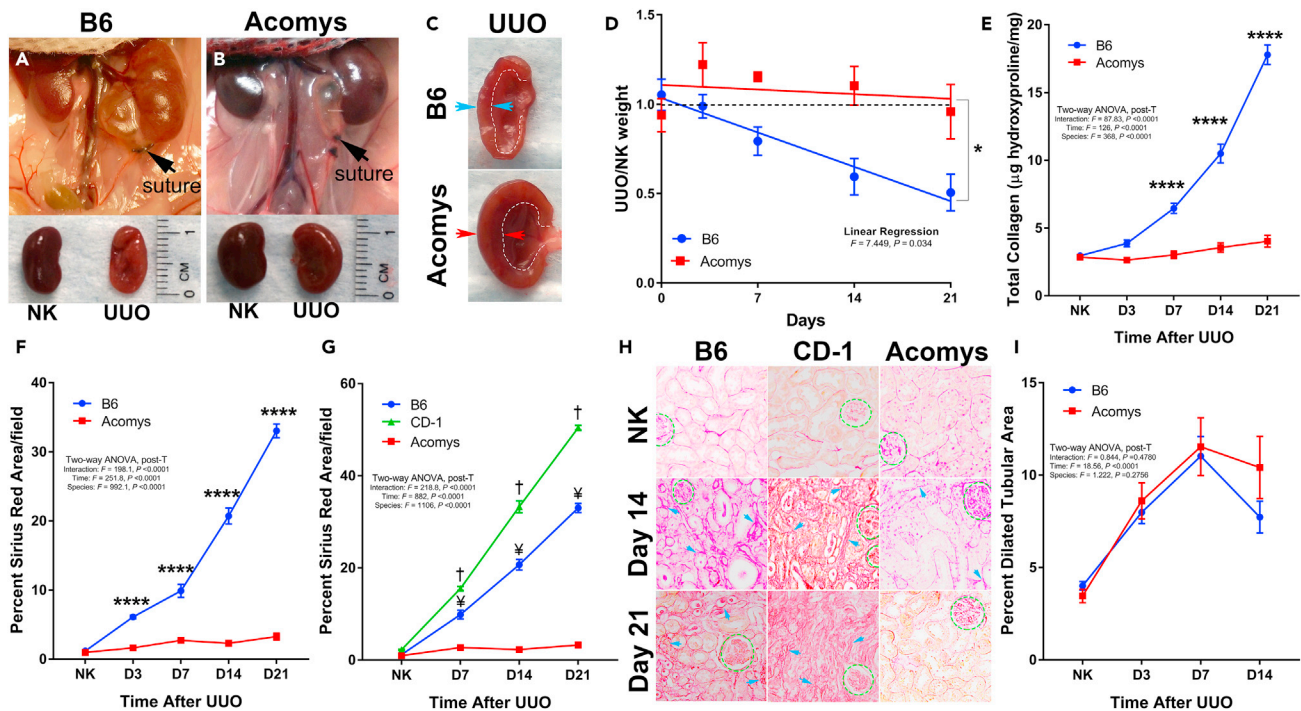


Figure 1. Absence of fibrosis after severe obstructive injury in Acomys

(A and B) (Upper) The ureter from the left kidney was ligated (arrow) to produce obstructive injury in both Acomys and C57BL/6J (B6) mice. (Lower) Upon gross inspection, contralateral kidneys (NK) from the two species are similar in length but Acomys UUO kidneys appear less damaged than B6 UUO kidneys after 14 days of obstruction.

(C) Panel demonstrates preservation of parenchymal thickness (greater distance between arrows) in Acomys kidney with renal pelvis noted by dotted white line.

(D) The graph demonstrates the best fit line of the ratio of UUO:NK kidneys for each time point, and the slopes were analyzed by linear regression (n = 6–10/time point).

(E) Total collagen content was measured by micrograms hydroxyproline per mg wet kidney weight. Graph summarizes total collagen measurement for B6 and Acomys NK and UUO kidneys (n = 6–8/time point for each group)

(F) Graph summarizes image analysis of picosirius red staining for each UUO time point (n = 6/time point for each group).

(G) UUO was performed on outbred CD-1 mice (green) (n = 3–4/time point), and the development of fibrosis was compared with B6 (blue) and Acomys (red).

(H) Graph summarizes image analysis of picosirius red staining with (H) representative digital images (400x). Glomeruli are outlined (dotted green). Arrows demonstrate Sirius red staining of interstitial matrix.

(I) Dilated tubular area was measured in Masson trichrome sections; graph summarizes image analysis of tubular dilation area in B6 and Acomys after UUO (n = 6–7/time point for each group). Data are represented as mean ± SEM. 400x field = 388 μm². B6 versus Acomys: *p < 0.05, **p < 0.01, ***p < 0.001, ****p < 0.0001; CD-1 versus Acomys: †p < 0.0001; B6 versus CD-1: ‡p < 0.0001.

unprecedented findings for adult mammalian kidney represent the first step to understand how wound healing evolved to be uncoupled from a robust fibrotic response to injury and redirected toward regeneration/complete repair of complex vital organ function in a terrestrial mammal, the spiny mouse.

RESULTS

Spiny mice fail to develop fibrosis after UUO injury

Tubulointerstitial fibrosis is the final common pathway of many forms of kidney disease (Duffield et al., 2013; Duffield, 2014; Humphreys, 2018). UUO is a reliable and aggressive model of chronic kidney injury that produces robust interstitial fibrosis. In previously reported studies where the contralateral kidney was removed after 7 days of obstruction in *Mus*, UUO kidneys were found to have about 50% function. After 14 days they become nonfunctional, resulting in 100% mortality from kidney failure (Tapmeier et al., 2008). We performed UUO surgeries on Acomys and *Mus* and retrieved injured kidneys (UUO) and contralateral uninjured normal kidneys (NK) at the times indicated (Figure 1). We found that even after 14 days of obstruction with obvious signs of hydronephrosis (Figures 1A and 1B), the gross anatomic structure and parenchymal thickness (between arrows, Figure 1C) were remarkably preserved in Acomys compared with *Mus*. This preservation of tissue structure

was confirmed by the maintenance of relatively normal kidney weights in obstructed *Acomys* kidneys compared with rapid declines in kidney weights in *Mus* as a result of progressive renal fibrosis (Figure 1D, ratio of slopes: $m_{Mus}/m_{Acomys} = -7.5$; $p = 0.03$). There were no significant differences in uninjured contralateral kidney weights between *Acomys* and *Mus* (data not shown).

Progression of fibrosis was monitored by three assays. Total collagen levels were determined biochemically as total hydroxyproline content. Kidney collagen levels increased rapidly in *Mus* whereas *Acomys* exhibited no significant change from the uninjured contralateral kidney (NK) ($n = 6-8$, Figure 1E). Remarkably, even out to 21 days of obstruction, there were no significant differences in total collagen levels between UO kidney and uninjured NK in *Acomys* ($n = 6-8$, Figure 1E). Computer-assisted image analysis of picrosirius red-stained kidney tissue sections demonstrated a nearly complete absence of interstitial matrix fibrosis at each time point after UO injury in *Acomys* even out to 21 days of obstruction (*Acomys*: NK versus 3d–21d, NS), compared with extensive interstitial fibrosis in *Mus* kidneys (Figures 1F and S1). Interstitial fibrosis, inflammation, and tubular atrophy (IFTA) were blindly scored on Masson's trichrome stained sections. We found that IFTA scores were markedly reduced in *Acomys* compared with *Mus* (B6) despite chronic obstructive injury in both species (Figure S2). In order to test our finding in an outbred strain of *Mus*, we performed UO surgeries on CD1 mice and measured fibrosis severity by picrosirius red staining.

Of interest, we found even more dramatic increases in interstitial fibrosis in CD1 mice, producing even greater differences in fibrotic tissue areas when compared with *Acomys* (Figures 1G and 1H; $p < 0.0001$). All together, these results demonstrate that, in contrast to either inbred or outbred *Mus* strains, *Acomys* preserved renal mass and did not develop fibrotic tissue in response to severe and chronic kidney injury.

Acomys maintains tubular integrity and represses myofibroblast accumulation after UO injury

To quantify the extent of obstructive tubular injury, we measured the dilated tubular area in *Acomys* and *Mus* at day 3 through day 14 after UO. As expected from the obvious hydronephrosis seen in Figures 1A and 1B, we found that tubular dilation increased significantly in both species following UO compared with the contralateral uninjured kidney and peaked at day 7 (Figure 1I; $p < 0.05$). Importantly, the extent of tubular dilation was not significantly different between *Acomys* and *Mus* throughout the time course examined (Figure 1I). Activated myofibroblasts (positive for smooth muscle α -actin, Acta2/SM α A) are a major source of collagen-rich extracellular matrix produced during kidney fibrosis. Chronic tubular injury is known to promote the production of intrarenal profibrotic cytokines that activate myofibroblasts (Grgic et al., 2014). Although SM α A immunolabeling increased after UO in both species, *Mus* exhibited higher levels of SM α A + myofibroblasts compared with *Acomys* (Figures 2A and 2B; $p < 0.01$). In contrast to the lack of fibrosis in *Acomys* after UO (Figures 1D and 1E), there was a significant increase in SM α A + myofibroblasts at day 14 after UO compared with NK and day 3 time points (Figure 2B, $p < 0.05$). These results suggest that the absence of interstitial matrix deposition in *Acomys* after UO injury is not due to the absence of myofibroblasts but rather species-specific differences in myofibroblast phenotypes. Chronic inflammation with a predominance of macrophages is a characteristic finding in organ injury and is strongly correlated with tissue fibrosis (Duffield, 2014). Similar to *Mus*, F4/80 + macrophages infiltrated *Acomys* kidneys after UO (Figure 2C). To quantify macrophage infiltration, whole kidneys were enzymatically digested into single-cell suspensions and analyzed for F4/80 expression by flow cytometry (Figure 2D). As expected, the number of F4/80 macrophages increased in *Mus* UO kidneys with advancing obstruction (days 7 and 14) compared with contralateral NK ($p < 0.001$). In comparing *Acomys* with *Mus* kidneys, significant reductions in F4/80⁺ macrophage content were found at each time point examined ($p < 0.05$) but less dramatic than seen in the fibrosis (Figures 1D and 1E) and myofibroblast (Figure 2B) data.

These results suggest that the unique absence of fibrosis in *Acomys* is not due to a complete absence of a chronic inflammatory response or an absence of myofibroblasts in injured kidney tissue but suggests evolutionary adaptations of these cell types in regenerative wound repair. Tubular integrity is strongly correlated with nephron function and can serve as a histological surrogate of whole kidney function (Liu et al., 2013; Chaabane et al., 2013). *Cdh1* (E-cadherin) is an indicator of tubular cell integrity and polarity whose expression is lost with ongoing obstructive injury, leading to loss of tubular architecture (Zheng et al., 2016). As expected for *Mus*, there was progressive loss of *Cdh1* expression with each time point after UO compared with the contralateral normal kidney (Figures 2E and 2F). However, in *Acomys* no significant changes in *Cdh1* protein levels with advancing obstructive injury were observed until day 14 compared with the

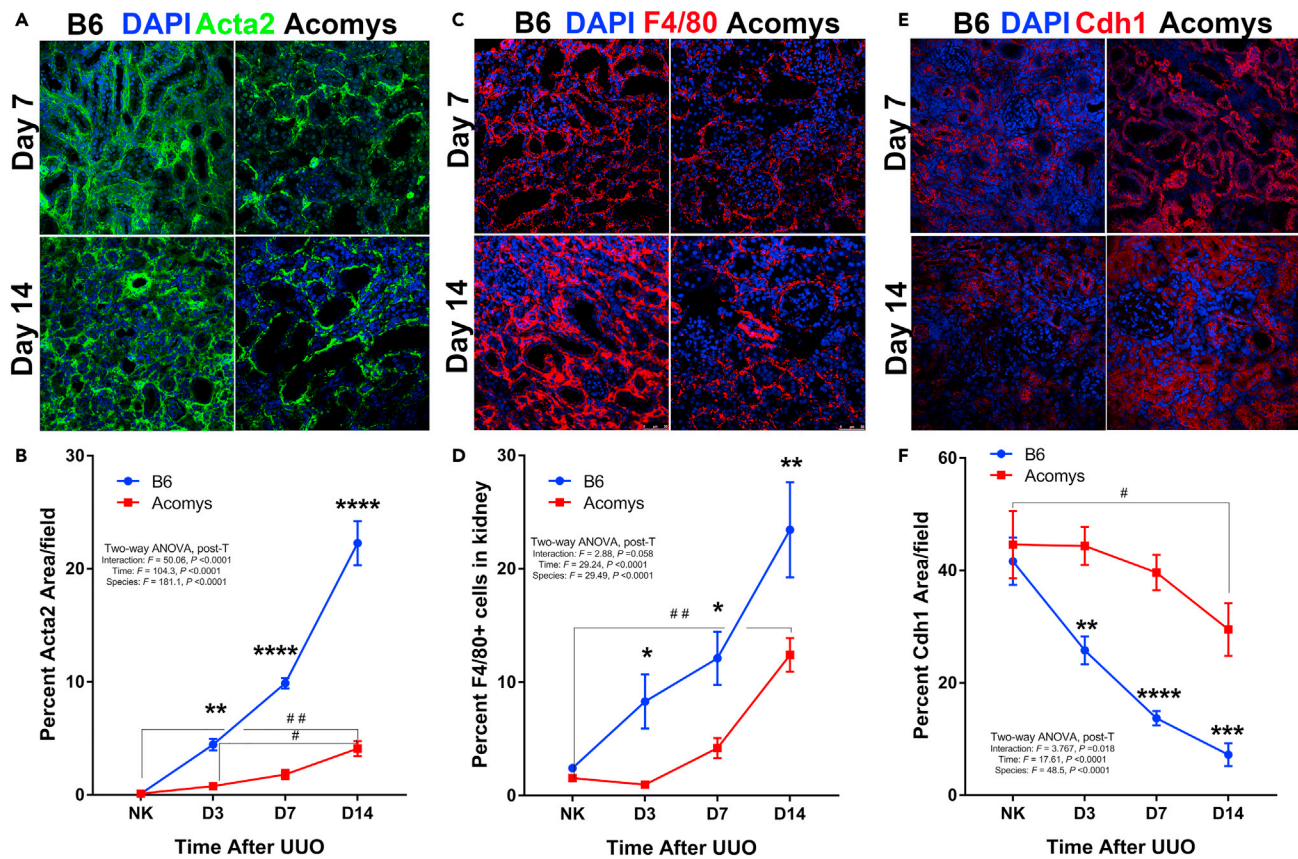


Figure 2. Myofibroblast formation and macrophage infiltration do not generate a fibrotic response in Acomys

(A) Smooth muscle alpha actin (Acta2/SM α A) expression was investigated by immune-confocal microscopy at days 3, 7, and 14 after UUO. Representative digital images (400x) SM α A expression (green) for B6 and Acomys at days 7 and 14 after UUO.

(B) Graph summarizes image analysis for SM α A at each time point (n = 6/time point for each group).

(C) F4/80 macrophage infiltration was examined by confocal microscopy and quantified by flow cytometry. Representative digital images (400x) of F4/80 (red) expression at days 7 and 14 after UUO.

(D) Flow cytometry was performed on single-cell suspensions from whole kidney and analyzed for F4/80 expression. Graph summarizes percent F4/80 + cells at days 3, 7, and 14 after UUO analyzed by FACS (n = 3–4/time point per group).

(E) Tubular integrity was examined by confocal microscopy for Cdh1 (E cadherin). Representative digital images (400x) of Cdh1 (red) expression for B6 and Acomys.

(F) Graph summarizes image analysis results for Cdh1 levels at each time point (n = 6/time point for each group). Data are represented as mean \pm SEM. 400x field = 388 μ m². B6 (blue) versus Acomys (red): *p < 0.05, **p < 0.01, ***p < 0.001, ****p < 0.0001; between time points #p < 0.05, ##p < 0.01.

contralateral uninjured kidney. There were no differences in Cdh1 expression levels in uninjured contralateral kidneys between Acomys and Mus (Figure 2F). Thus, despite severe chronic obstruction, Cdh1 protein levels were maintained in Acomys while becoming significantly decreased in Mus. Altogether, these results demonstrate that despite equivalent tubular dilation with obstruction (Figure 1I), significant attenuations in myofibroblast activation, macrophage infiltration, and Cdh1 protein loss were found in Acomys kidneys that correlated with preservation of tubular integrity and absence of interstitial fibrosis when compared with Mus.

Initial injury response transcriptomes in Acomys correlate with regeneration

In order to further delineate the differences in initial responses to tissue injury between Acomys and Mus, we carried out RNA seq analysis on whole kidneys. We compared transcriptional responses at days 2 and 5 in Acomys kidneys versus Mus kidneys after UUO. We aligned our Acomys dataset to existing spiny mouse transcriptomes (Mamrot et al., 2017) and identified 1700–2500 Acomys differentially regulated loci across sham and injured groups, which principal component analysis (PCA) revealed as distinct datasets (Figure S3A). We successfully mapped 77% of Acomys differentially regulated transcripts between day

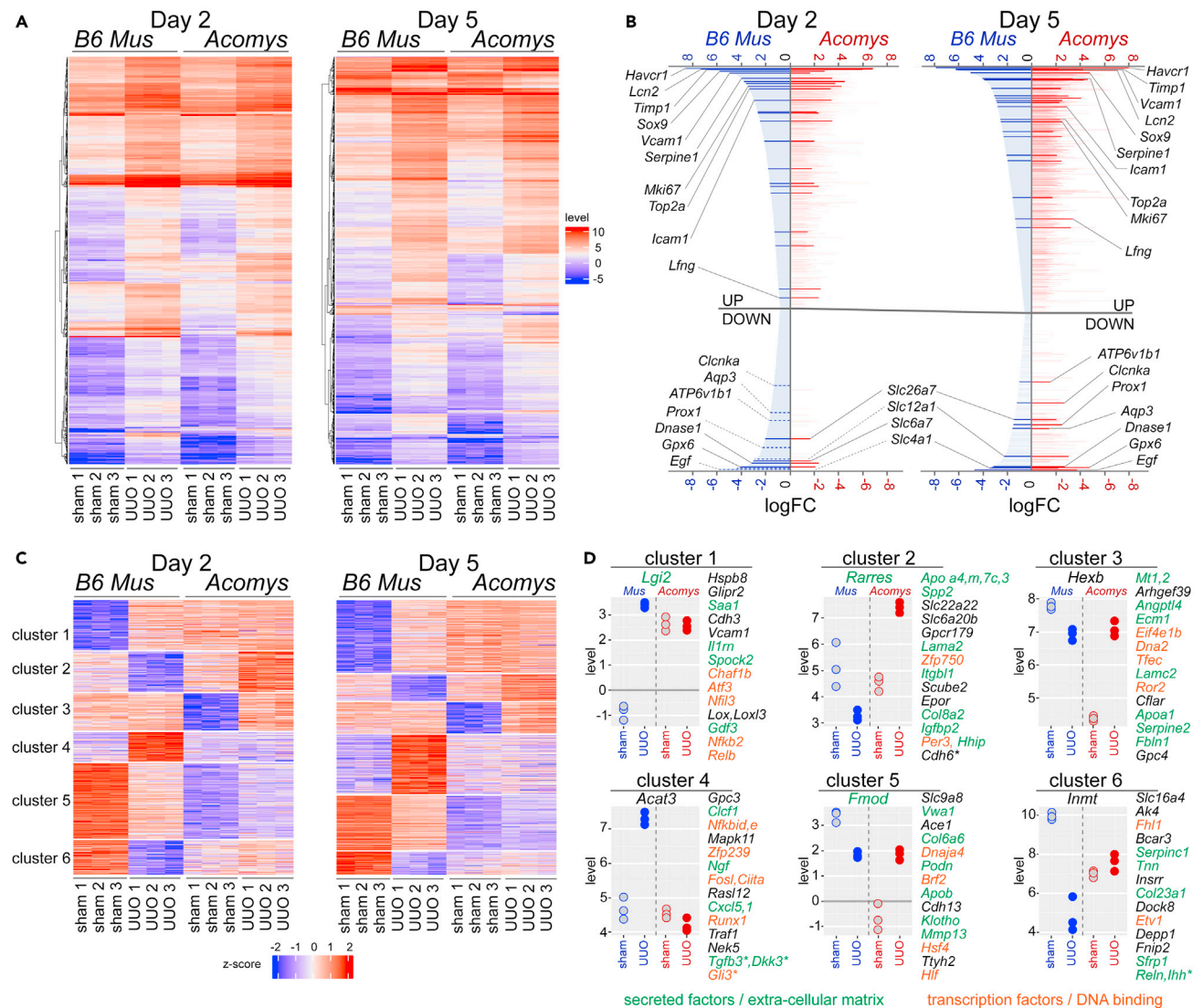


Figure 3. Transcriptome cluster analysis reveals conserved injury response and unique reparative gene sets in Acomys

Total RNA was obtained from sham and UJO kidney samples at days 2 and 5 in B6 and Acomys and examined by RNA Seq analysis (n = 3/group). Comparative analysis of differentially expressed RNA Seq transcripts with an FDR <0.05, and a 1.5 linear fold change (logFC >0.585) from B6 and Acomys demonstrated overlapping and nonoverlapping gene subsets (Figure S3C).

(A) Heatmaps between both species revealed similar overall patterns of expression at days 2 and 5 after UJO despite dramatically different fibrosis outcomes.

(B) Overlapping genes between B6 and Acomys demonstrated expected upregulated injury response, matrix, and inflammation genes and downregulated transport channels and enzymes. For nonoverlapping genes, we performed an interaction analysis on differentially expressed transcripts between species based on its mean group expression level (FDR <0.05 and a 1.5 linear fold change) to indicate a distinct species-specific gene expression change.

(C) Interaction analyses revealed 6 clusters of genes that were differentially expressed with UJO injury (Sham:UJO) between Mus and Acomys at days 2 and 5 datasets.

(D) Representative graphs of cluster genes from day 2 and day 5 datasets indicate the most significant gene in each cluster at the top with their pattern of expression below. Notable and novel genes for the cluster are noted on the sides of the graph (green: secreted factors and matrix proteins; red: transcription factors or DNA binding protein; black: other; *5d only).

2/sham and day 5/sham UJO datasets to identifiable mouse genes (Figure S3B), which were used in subsequent analyses. Comparisons between species for day 2 and day 5 datasets revealed extensive overlap between *M. musculus* and Acomys initial transcriptional responses to injury, predominantly in upregulated genes (Figure S3C). Within the overlapping dataset (Figure S3) there were largely conserved transcriptional responses to tissue injury between Mus and Acomys at both day 2 and day 5 (Figure 3A). Further analysis of

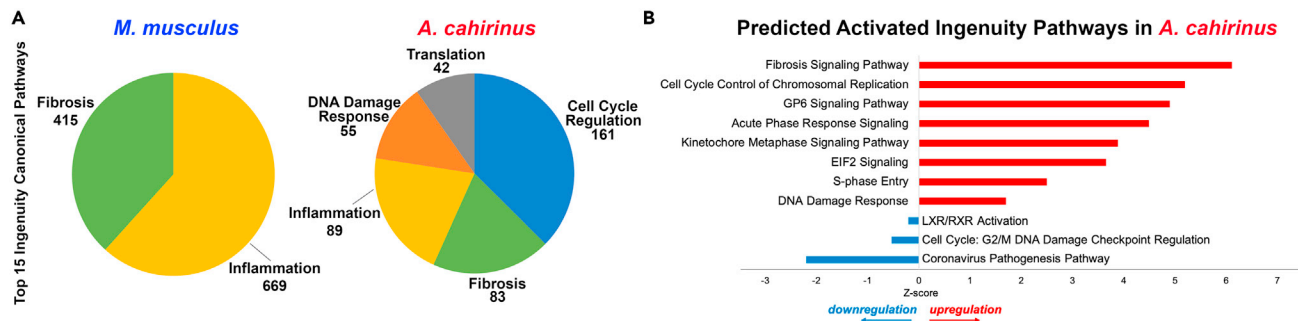


Figure 4. Ingenuity pathway analysis identifies differences in gene regulation early after UUO injury in *Acomys*

Differentially expressed transcripts between sham and UUO kidneys at day 2 from B6 and *Acomys* were analyzed by IPA. The top 15 most significant differentially regulated canonical pathways fit within five main categories: inflammation, fibrosis, cell-cycle regulation, translation, and DNA damage response.

(A) The charts demonstrate the relative fraction of total genes identified that are represented in each pathway in the category with the number of genes listed beneath. IPA activation Z score predicts the activation state of the canonical pathway using the gene expression patterns of the genes within the pathway. (B) In *Acomys* cell-cycle control and DNA damage response are among the top biologically activated pathways compared with fibrosis and inflammation in *Mus* (Figure S5).

genes (>1 log CPM) in this conserved response to injury identified the upregulation of typical markers of kidney injury, including *Havcr1* (*Kim1*), *Lcn2* (*Ngal*), *Timp1*, *Sox9*, *Vcam1*, *Serpine1*, and *Icam1*, after UUO (Figure 3B). Although fewer downregulated genes were identified in *Acomys* compared with *Mus*, they showed a similar pattern affecting ion transport genes in the distal segments of the nephron (*Clnka*, *Aqp3*, *ATPV6v1b1*, *Slc26a7*, *Slc12a1*, *Slc4a1*) and enzymes (*Dnase1*, *Gpx6*) (Figure 3B). These data demonstrated there were many conserved responses to kidney injury between *Mus* and *Acomys* despite the divergent outcomes for interstitial fibrosis and kidney function.

To identify potential differences in transcriptional responses to kidney injury leading to scarless regenerative repair in *Acomys*, we considered whether any gene in the nonoverlapping dataset (Figure S3C) exhibited a statistical interaction difference from its mean group expression level (FDR <0.05 and a 1.5 linear fold change) that could indicate a distinct species-specific change in gene expression (*Acomys* relative to *Mus*). This analysis resulted in 843 genes between day 2 and day 5 groups (Figure 3C). Interaction analyses of day 2 and day 5 datasets revealed 6 clusters of genes that were differentially regulated with UUO injury (sham:UUO) between *Mus* and *Acomys* (Figure 3C). For example, cluster 1 contains a set of injury response genes that are upregulated after UUO in *Mus* but in *Acomys* exhibit increased expression in sham but do not significantly change after UUO. Hence, clusters 1 and 4 represent *Mus*-specific genomic responses to UUO injury (i.e. upregulated genes), whereas the response to injury in *Acomys* is to maintain expression of these genes at homeostatic levels (equal to sham). Examination of the expression level for the top gene in cluster 1 (*Lgi2*) and cluster 4 (*Acat3*) illustrate the general pattern for other cluster members, many of which are secreted factors, cytokines, transcription factors, or DNA-binding chromatin modifiers (Figure 3D). Interestingly, profibrotic and myofibroblast-inducing factors upregulated by UUO in *Mus* in cluster 4 (*Tgfb3*, *Dkk3*, *Runx1*, *Gli3*, *Nkd2*) were not significantly changed from sham levels in *Acomys*. In addition, a concerted upregulation of inflammatory mediators in *Mus* in cluster 1 (*Atf3*, *Nfil3*, *Nfkb2*, *Relb*) and cluster 4 (*Nfkbid*, *Nfkbie*, *Ciita*) were also unchanged from sham in *Acomys*. These clusters suggest that the response to kidney injury in *Acomys* involves downregulation of the responsiveness of critical profibrotic and inflammatory mediators that drive myofibroblast accumulation and interstitial fibrosis in *Mus* (Figure 3D). In contrast, clusters 2 and 3 represent *Acomys*-specific kidney response gene sets (upregulated with UUO), as they are unchanged or downregulated in *Mus*. In order to investigate the drivers of the transcriptional responses in *Acomys*, we performed a transcription factor enrichment analysis (Keenan et al., 2019) on the genes from clusters 2 and 3 (Table S1). Of the top 10 transcription factors from this analysis, many were involved in regulation of cell-cycle activity and five were significantly upregulated in *Acomys* at day 2 (*Cenpa*, *Mybl2*, *Dnmt1*, *Foxm1*, *Znf367*). Ingenuity pathway analysis (IPA) was performed on day 2 differentially expressed transcripts between *Mus* and *Acomys* (Figure 4). Although the analysis is somewhat limited by the incomplete identification of the full set of differentially regulated genes in *Acomys*, the pathways were markedly distinct. We examined the top 15 canonical pathways identified by IPA and categorized them for both species (Table S2); this demonstrates the difference in response to chronic injury

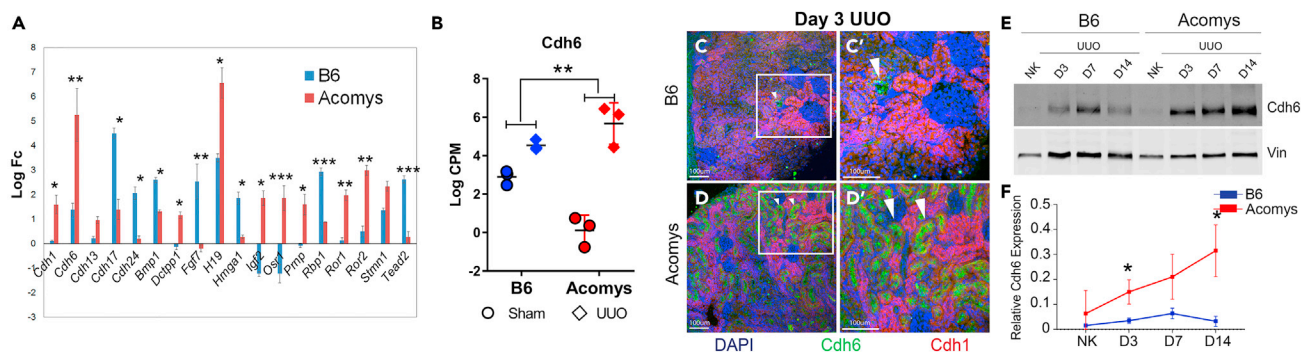


Figure 5. Acomys injury response gene cluster reveals nephrogenic progenitor profile

Significant differentially expressed genes (FDR <0.05, 1.5 linear fold change) in nonoverlapping gene set segregated into six unique clusters (n = 3/group). (A) Graph summarizes log fold change (log Fc) between UUO and Sham for day 5 for established nephrogenic progenitor genes; blue: B6, red: Acomys. (B) Graph summarizes RNA Seq gene expression of *Cdh6* at day 5 after UUO; circle: sham, diamond: UUO. (C and D) Representative digital images (400x) of *Cdh6* (green) and *Cdh1* (red) expression at day 3 after UUO. (400x; scale bars, 100 μ m). (C') High-powered (630x) digital image demonstrates small *Cdh6* population (arrow) in B6 UUO kidney; and (D') expanded *Cdh6* subpopulation (arrows) distinct from *Cdh1* mature tubular cells in Acomys UUO kidney. (E) Representative western blot demonstrates increased *Cdh6* protein expression in Acomys with each UUO time point. (F) Graph below summarizes normalized *Cdh6* protein levels after UUO (n = 4/group/time point). Data are represented as mean \pm SEM. B6 versus Acomys: *p < 0.05, **p < 0.01, ***p < 0.001.

between the species: a regenerative response (cell-cycle regulation and DNA damage response) predominated in Acomys compared with inflammation and fibrosis in Mus (Figures 4A and 4B). Consistent with our tissue analysis, common pathways between both species included fibrosis/myofibroblast activation, acute phase response, and fibrosis signaling and confirmed that the key processes associated with fibrogenesis are present in Acomys at the RNA level (Figure S4). However, the pathways that are unique to Acomys are strongly activated (Figures 4B and S5) and, in combination with our functional outcome of no fibrosis, suggested that they are critical to the regenerative response.

Based on the regenerative potential of Acomys, we investigated the expression of established nephrogenic genes (Hendry et al., 2011; O'Brien and McMahon, 2011; Oxburgh, 2018; Adam et al., 2017) in clusters 1–6. We found several differentially regulated nephron progenitor genes selectively induced in Acomys (Figure 5A). Especially interesting were the genes from cluster 3 (*Cdh1*, *Cdh6*, *Osr1*, *Ror1*, *Ror2*, and *Stmn1*) that are upregulated in Acomys after UUO but not in Mus. Furthermore, cluster 2, the other Acomys kidney response gene cluster, contained genes *Igf2* and *H19* that have been linked to persistence of nephron progenitors (Yermalovich et al., 2019) and to angiogenesis (Haddad et al., 2021). To validate the RNA seq analysis, we chose *Cdh6* because it was the most highly differentially regulated among the nephron progenitor genes (Figure 5B). *Cdh6* is strongly expressed in nephron progenitor cells during kidney development and then downregulated after birth (Mah et al., 2000). During nephrogenesis, *Cdh6* is expressed in mesenchymal aggregates, renal vesicle, and proximal tubule progenitors (Cho et al., 1998). *Cdh6* is strongly expressed in the nephrogenic zone where mesenchymal-to-epithelial transition is occurring and becomes downregulated in mature proximal tubular cells (Cho et al., 1998). At day 3 after UUO, *Cdh6* is confined to a small subset of tubules in Mus (Figures 5C and 5C'); however, there was striking reexpression of *Cdh6* in mosaic patches throughout the proximal tubular network in Acomys with little or no overlap with *Cdh1*-positive tubular cells (Figures 5D and 5D' arrows). Western blot analysis confirmed significantly increased protein levels of *Cdh6* in UUO kidneys with a 5-fold increase at day 14 in Acomys compared with Mus (Figures 5E and 5F). Taken together, the reactivation of nephrogenic progenitor gene expression after injury in Acomys suggests a mechanistic basis for regeneration of kidney mass without fibrosis. Thus, despite the activation of typical injury response genes in Acomys, the net effect is a reprogramming of the cellular response to injury toward cell-cycle control and DNA damage responses that drives a regenerative program, leading to a completely different wound healing outcome when compared with that observed in Mus.

Assessment of kidney structure and function after ischemia-reperfusion injury

Although the UUO model is useful in the study of experimental renal fibrosis in animals, it is of limited relevance to human kidney disease. Ischemia-reperfusion is a more relevant model of acute necrotic kidney injury followed by maladaptive repair typically observed in humans. In order to provide a stringent test

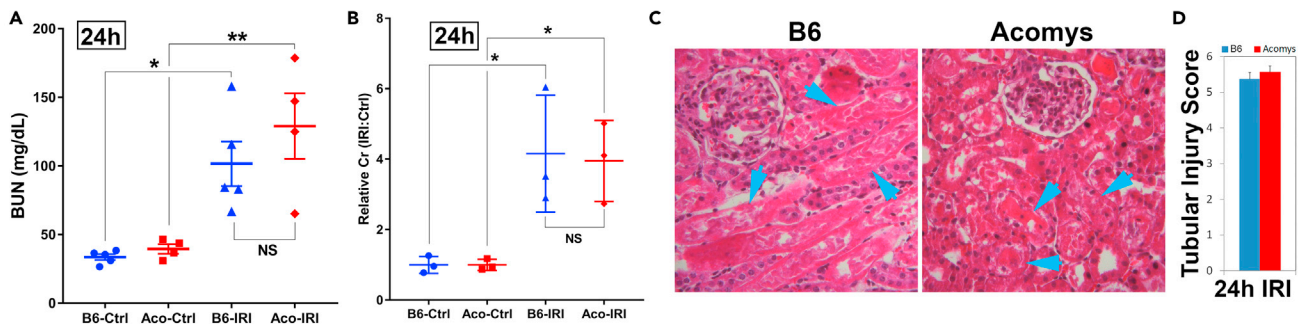


Figure 6. Acute ischemic reperfusion causes equivalent histologic and functional injury in both species

B6 and *Acomys* underwent unilateral IRI (uni-IRI) with contralateral nephrectomy and sacrificed at 24 h.

(A) Graph summarizes BUN levels were assessed in uninjured animals (Ctrl) and those sacrificed at 24 h (n = 4–5/time point per group); body weight of *Acomys* is 2–3 times higher than B6 with higher normal creatinine (Cr) levels. Relative creatinine (Cr) ratios (IRI/Ctrl) were used as a second measure of kidney function.

(B) Graph summarizes relative Cr ratios in Ctrl and 24 h IRI animals. Note that both species exhibited equivalent severe acute kidney damage in response to ischemic injury.

(C) H&E-stained sections were blindly scored for tubular injury (see STAR Methods, n = 4–5/group); representative H&E digital images (400x) at 24 h from IRI kidneys. Arrows indicate tubular casts and necrotic cell debris.

(D) Graph summarizes tubular injury scores at 24 h after IRI.

Data are represented as mean \pm SEM. B6: blue; *Acomys*: red; Ctrl: circle, square; IRI: triangle, diamond; NS: not significant. *p < 0.05, **p < 0.01.

of *Acomys* capacity for scarless, regenerative repair of kidney injury, we produced severe ischemic injury by clamping the renal vasculature for 40 min followed by reperfusion of the ischemic kidney (Liu et al., 2017). To quantify the extent of initial injury, we performed uni-IRI with a simultaneous contralateral nephrectomy (uni-IRI-Nx) on *Acomys* and *Mus* and sacrificed them at 24 h after surgery in order to correlate whole organ kidney function with histology after severe acute injury. We found dramatic elevations in blood urea nitrogen (BUN) levels 24 h after uni-IRI + Nx in both species, indicating acute loss of kidney function (Figure 6A). Importantly, these elevated BUN levels were not significantly different between *Acomys* and *Mus*. In fact, there was a trend toward higher BUN levels in *Acomys* (BUN: *Mus* versus *Acomys*, 102 ± 16 versus 129 ± 24 mg/dL). We also measured serum creatinine and found this independent assay of kidney function was also acutely elevated after IRI compared with control with no difference between species after IRI (Figure 6B). H&E sections on the Uni-IRI-Nx kidneys from *Acomys* and *Mus* at 24 h were analyzed for tubular cell necrosis, tubular casts, and dilation and assigned cumulative tubular injury scores. Consistent with our kidney function data at 24 h, we found equivalent and extensive damage to tubular structures in both species at 24 h after IRI (Figures 6C and 6D). Therefore, consistent with our transcriptome data, both species experience acute kidney injury and tissue damage to equal extents after prolonged renal ischemia as assessed both histologically and functionally.

Regeneration of tubular damage after ischemia-reperfusion injury in *Acomys*

As a first step to investigate the ability of *Acomys* to regenerate kidney structure and function after acute kidney injury, we performed uni-IRI without contralateral nephrectomy to allow long-term survival in both species and then sacrificed animals at day 14 to assess kidney structure by histology. Similar to our UUO study, there was a robust preservation of kidney tissue mass following severe ischemic injury by IRI in *Acomys* compared with progressive decline in kidney tissue mass in *Mus* (Figure 7A). At day 14 after IRI, ischemic/contralateral kidney weight ratios were maintained in *Acomys* (0.92 ± 0.01) compared with almost 40% loss of renal parenchymal mass to fibrosis in *Mus*. (0.64 ± 0.05). Remarkably, despite severe acute ischemic injury, we found a complete absence of fibrosis by picrosirius red staining in *Acomys* compared with either B6 or CD1 strains of *M. musculus* (Figures 7B and 7C). Acute tubular injury leads to activation and accumulation of myofibroblasts. In *Mus*, Acta2/SM α A immunolabeling progressively increased with time after IRI, whereas in *Acomys*, SM α A⁺ myofibroblasts plateaued at day 7 and were significantly less abundant at day 14 compared with *Mus* (Figures 7D and 7E; p < 0.0001). Interestingly, despite similar ischemic injury F4/80 + macrophage infiltration was significantly decreased in *Acomys* compared with *Mus* (Figure S6). Consistent with an equivalent initial injury after IRI, there was a similar loss of Cdh1 in both species at day 7 (Figures 7F and 7G). However, at day 14, *Acomys* was able to regenerate mature tubular epithelium with Cdh1 immunostaining returning to baseline levels, whereas Cdh1 expression

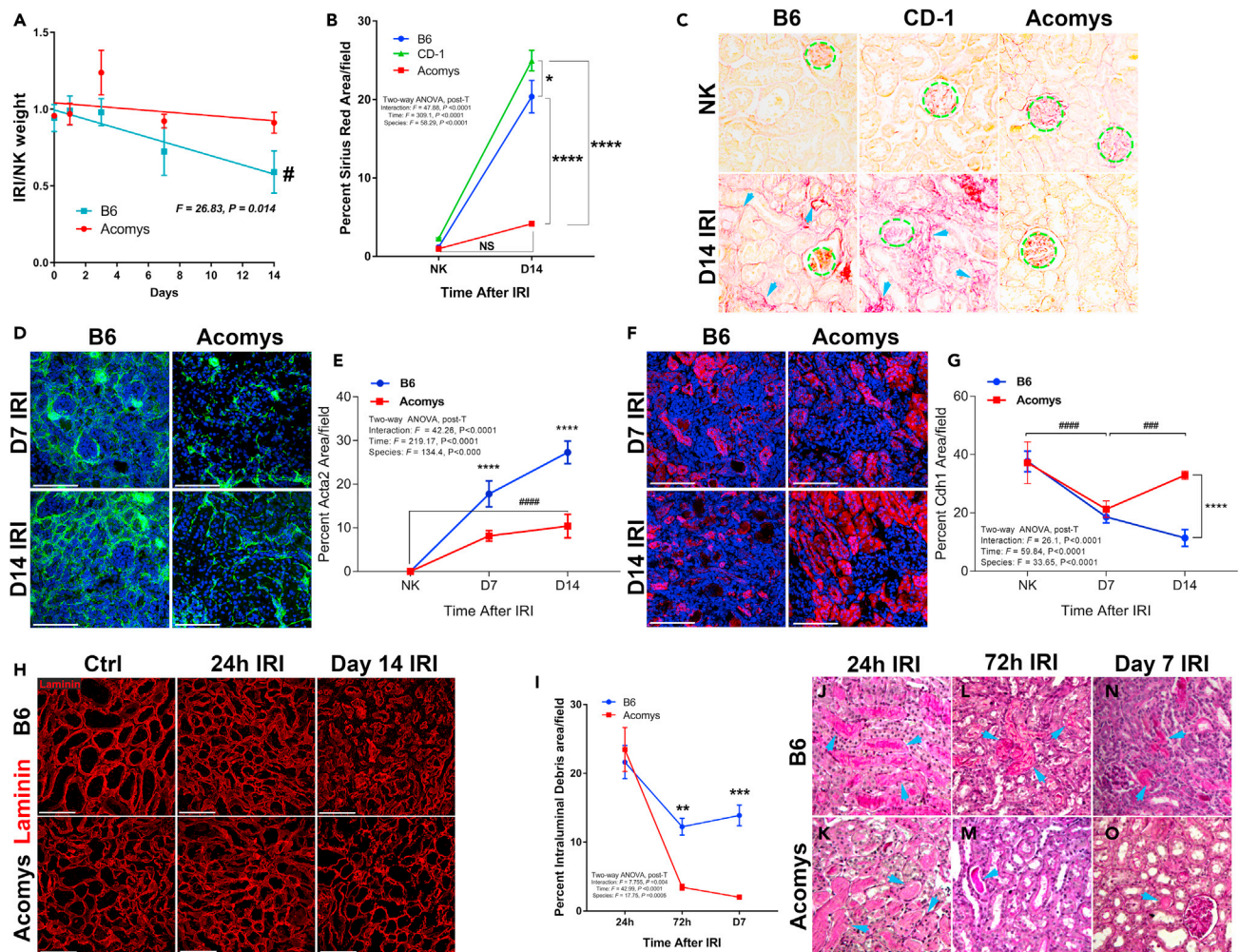


Figure 7. Regeneration of nephron architecture after severe ischemia reperfusion injury in Acomys

In order to determine effect of acute injury on regeneration, uni-IRI was performed on B6, CD-1, and Acomys.

(A) Graph summarizes data on IRI/contralateral (NK) kidney weight ratio at time of sacrifice (n = 4–6/group): *p < 0.05, **p < 0.01.

(B) Graph summarizes image analysis of picosirius red staining for each IRI time point (n = 5–6/time point for each group); B6 (blue), CD-1 (green), Acomys (red): *p < 0.05, ****p < 0.0001.

(C) Representative picosirius red digital images (400x). Glomeruli are outlined (dotted green). Arrows demonstrate Sirius red staining of interstitial matrix.

(D) Smooth muscle alpha actin (Acta2/SM α) expression was investigated by immunofluorescence-confocal microscopy at days 7 and 14 after uni-IRI.

Representative digital images (400x) of SMA α expression (green) for B6 and Acomys at days 7 and 14 after uni-IRI.

(E) Graph summarizes image analysis for SM α A at each time point (n = 4–5/time point for each group).

(F) Tubular integrity was examined by confocal microscopy for Cdh1. Representative digital images (400x) of Cdh1 (red) expression for B6 and Acomys.

(G) Graph summarizes image analysis results for Cdh1 levels at each time point (n = 4–5/time point for each group).

(H) Laminin (red) immunostaining of tubular epithelial basement membrane architecture at day 0, 24 h, and 14 days after IRI injury (400x; scale bars, 100 μ m).

Note Acomys kidney at day 14 (D14 IRI) strongly resembles uninjured kidney (Ctrl) in tubular basement membrane architecture, whereas B6 basement membranes demonstrate collapse and thickening with advancing fibrosis. Scale bars, 100 μ m. Tubular casts and debris were identified on Periodic acid Schiff (PAS) stain in unilateral IRI kidneys at 24 h, 72 h, and 7 days in B6 and Acomys (I, J–O).

(I–O) (I) Graph summarizes image analysis results for tubular casts and intraluminal debris after IRI. Representative fields from 200x images demonstrate representative tubular casts and intraluminal debris (arrow) in IRI kidneys at 24 h (J and K), 72 h (L and M), and 7 days (N and O) in B6 and Acomys kidneys. Arrows demonstrate areas of intraluminal debris/casts. Data are represented as mean \pm SEM. 400x field = 388 μ m². B6 (blue) versus Acomys (red): *p < 0.05, **p < 0.01, ***p < 0.001, ****p < 0.0001; between time points #p < 0.05, ##p < 0.01, ###p < 0.001, ####p < 0.0001.

progressively declined by day 14 in *Mus* (Figures 7F and 7G; p < 0.0001). Likewise, staining for the tubular basement membrane protein laminin showed progressive shrinking and thickening by day 14 in *Mus* kidney consistent with tubular atrophy, whereas basement membrane structures at day 14 in *Acomys* strongly resembled normal uninjured kidney (Ctrl) (Figure 7H). The removal of necrotic and cellular debris after

injury is an important component of wound repair and tissue regeneration (Duffield, 2014). Intraluminal casts and debris were quantitated from kidney sections. This analysis revealed that both species exhibited equivalent levels of tubular casts/debris at 24 h after IRI (Figures 7I–7K, arrows). At later time points, *Mus* retained this intraluminal debris, whereas *Acomys* efficiently cleared it from the tubular network (Figures 7L, 7M, and 7O, arrows).

We then employed light sheet fluorescence microscopy (LSFM) to determine whether *Acomys* kidneys exhibited anatomical defects 14 days after IRI. We took advantage of the inherent autofluorescence signal generated by formaldehyde-based protein cross-linking to analyze structural changes throughout the entire kidney and especially the tubular casts (Leischner et al., 2015; Dodt et al., 2007). In undamaged *Mus* and *Acomys* kidneys, high-density protein-protein cross-linked structures generated similar high-contrast structure signals (tubules, ECM) compared with lower density structures (glomeruli, renal pelvis) and empty blood vessel lumens (Figure S7A). Consistent with our tubular cast data (Figure 7I), there was a persistence of tubular casts within the whole kidney in *Mus* at 14 days after IRI compared with a near-complete resolution of tubular casts in *Acomys* (Figure S7B). Although there were similar levels of tubular necrosis and tubular casts seen in the corticomedullary junction at 24 h after severe IRI in both species (Figure 6C), what was strikingly different in *Acomys* was the abundance of polymorphonuclear cells and other nucleated cells within intraluminal tubular casts that was seen much less frequently in *Mus* (Figures S8A–S8E, arrows). Consistent with our quantitative data (Figure 7I), by 72 h tubular casts, dilation, and interstitial inflammation progressed in *Mus* (Figures S8F and S8G), whereas in *Acomys* the intraluminal cellular debris had been removed and replaced by highly nuclear, somewhat disorganized tubular structures (Figure S8H), with flattened epithelial cells suggesting progression to/from a more dedifferentiated state (Figures S8I and S8J; arrows). By day 7, tubular damage and interstitial fibrosis continue to progress in *Mus* (Figures S8K and S8L) compared with the appearance of defined tubular structures with open lumens in *Acomys* (Figures S8M and S8N) and reestablishment of brush border structures in more mature differentiated tubular epithelial cells (Figures S8O) consistent with the increase in *Cdh1* (Figures 7F and 7G).

Complete regeneration of kidney function after IRI in *Acomys*

To compare the degree of nephron function with structural regeneration in the uni-IRI damaged kidney, we performed uni-IRI followed by a contralateral nephrectomy at day 14 and then measured kidney function over the next 2 days. Importantly, we found striking and reproducible differences in day 16 BUN levels between *Acomys* and *Mus* (Figure 8A). Consistent with a complete absence of interstitial fibrosis (Figure 7B) and restoration of mature tubular epithelium (Figures 7F and 7G) by day 14, we found that BUN levels had returned to normal values in *Acomys* indicative of complete regeneration of kidney function by 16 days after IRI (compare Figures 7B–7O and 8A). By contrast, *Mus* BUN levels were substantially increased indicative of progressive renal failure (Figure 8A). Relative changes in serum creatinine were also severely elevated in *Mus* after IRI and were restored to control levels in *Acomys* after IRI (Figure 8B).

Finally, in order to investigate the cellular basis of the regenerative response after severe IRI, we performed pulse labeling with EdU nucleoside every 2 days in *Mus* and *Acomys* with sacrifice at day 14. Surprisingly, there were no differences in total proliferating cells between *Acomys* and *Mus* at day 14 (Figures 8C–8E and 8I). However, consistent with the regeneration of nephron structure and function in *Acomys*, we found a 2.4-fold increase in proliferation in the proximal tubular compartments (*Cdh1*-positive) of the kidney (Figures 8H and 8I). In striking contrast to *Mus*, there was a substantial 20-fold increase in the number of ZO-1/Tjp1-positive glomerular cells (podocytes) after IRI in *Acomys* compared with *Mus* (Figures 8E, 8F, and 8I). The proliferation of podocytes strongly suggested that *Acomys* regenerated the glomerular compartment in addition to the tubular epithelium. In contrast, in *Mus* the predominant proliferating compartment emanated from the *Cdh1*- and *Tjp*-negative (other) subpopulation, which was primarily composed of interstitial cells and likely myofibroblasts. Both *Cdh6* and *Osr1* were significantly increased in the *Acomys* IRI kidney early after injury compared with little expression in *Mus* (Figures S9A–S9J). Interestingly, *Cdh6* and *Osr1* appear to be co-expressed in the same cells in the *Acomys* IRI kidney (Figure S9H). These unprecedented findings confirmed that the response to severe acute kidney injury in *Acomys* does not lead to the progressive, degenerative fibrotic response characteristic of mouse and human kidneys, but instead strikingly results in the complete regeneration of nephron structure and function with no fibrosis.

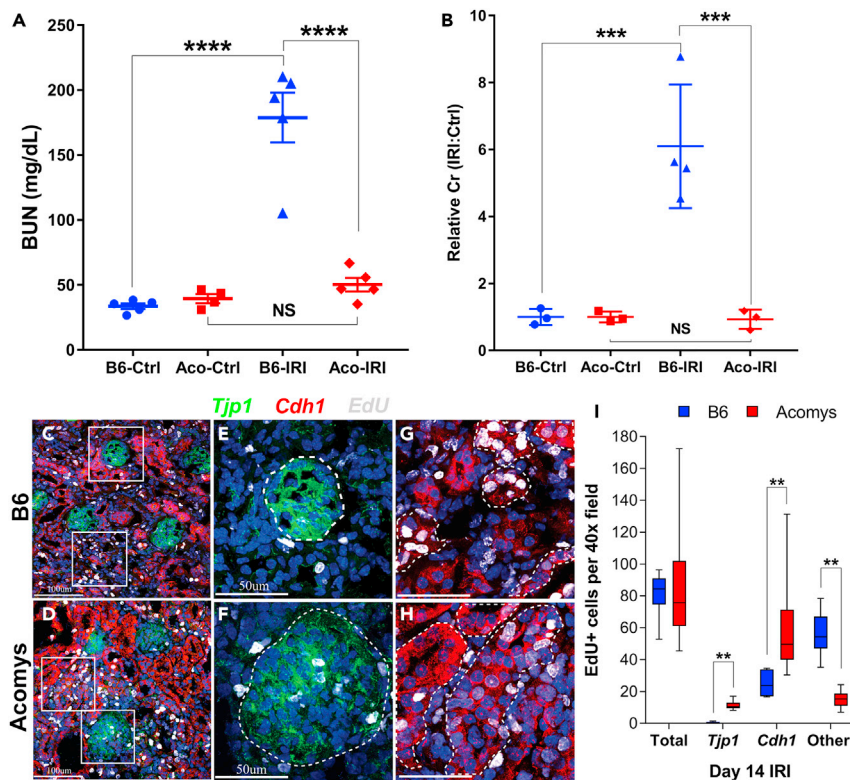


Figure 8. Restoration of nephron function after severe ischemia reperfusion injury through regeneration of glomerular and tubular compartment

In order to determine functional recovery, uni-IRI was performed, the contralateral kidney was removed at day 14, and kidney function was monitored until sacrifice at day 16.

(A) Graph summarizes BUN levels were determined in uninjured animals (Ctrl) and those sacrificed at 1 day 6, 2 days after contralateral nephrectomy (IRI). Note the complete recovery of nephron function in the injured *Acomys* kidneys at day 16 compared with the high BUN levels indicative of kidney failure in *B6* injured kidneys.

(B) Graph summarizes relative creatinine levels in *B6* and *Acomys* at day 16 confirming findings in graph (A). In order to identify proliferating subpopulations after IRI, animals were pulsed with EdU every 2 days starting at the time of surgery. (C–H) (C and D) Representative digital images (400x) of proliferating populations, EdU+ (gray), (400x; scale bars, 100 μ m) (E and F) podocytes/glomerular, ZO-1/Tjp1 (green) (scale bars 50 μ m), and (G and H) proximal tubular compartment, Cdh1 (red) (scale bars, 50 μ m). Note podocytes proliferating in *Acomys* after injury but not in *B6*.

(I) Graph summarizes image analysis results for total proliferating cells (EdU+), proliferating podocytes (EdU + Tjp1+), proximal tubular cells (EdU + Cdh1+), and other (EdU + Tjp1– Cdh1–).

Data are represented as mean \pm SEM. 400x field = 388 μ m². *B6*: blue, *Acomys*: red; *B6* versus *Acomys*: NS: not significant, ** p < 0.01, *** p < 0.001, **** p < 0.0001.

DISCUSSION

Restoration of solid organ architecture and function after injury or disease remains the holy grail of regenerative medicine. Using two different and highly aggressive forms of experimental kidney injury that produce organ failure due to renal fibrosis in *Mus*, we show that there was an absence of fibrotic tissue and a remarkable regeneration of kidney morphology and nephron function in *Acomys* compared with either inbred (*B6*) or outbred (*CD1*) strains of *Mus*. These striking differences in wound healing responses were not due to the failure of our injury models to produce acute organ damage in *Acomys* kidneys because histological and functional assays along with conserved injury response transcriptomes demonstrated equivalent tissue injuries in the first 24–48 h after UUO or IRI surgeries in both species. Yet within the milieu of common tissue damage, we observed that unique gene clusters were rapidly activated in surviving resident cells in *Acomys* kidney that included embryonic nephrogenic and angiogenic pathways that aligned with the subsequent regeneration of kidney architecture and function without fibrosis; this suggests that the spiny mouse genome is poised to rapidly initiate scarless wound healing in the adult kidney.

Muroid rodents of the genus *Acomys* (spiny mice) have evolved the ability to shed their dorsal skin to avoid predation and then to completely regenerate the lost skin tissue without fibrosis or scar formation (Seifert et al., 2012; Brant et al., 2015; Gawriluk et al., 2016; Matias Santos et al., 2016; Jiang et al., 2019). Mechanical and histological assays showed that *Acomys* skin is specialized to be structurally fragile and prone to tear under low tensile forces (Seifert et al., 2012). It, therefore, cannot be assumed *a priori* that the regenerative response to tissue injury in the skin, the first target of predatory attacks in the wild, necessarily extends to internal organs in *Acomys* species. A similar ear skin regenerative response was previously reported for the MRL/MpJ strain of mice (Clark et al., 1998). However, multiple attempts to determine if regenerative wound healing extended to internal organs, including kidneys, of these mice provided little or no support for this idea (Oh et al., 2004; Robey and Murry, 2008). Thus, our results on the striking absence of fibrotic tissue formation and the complete regeneration of nephron function in *Acomys* kidney suggest that the regenerative wound healing response previously described in the skin (Seifert et al., 2012; Brant et al., 2015; Gawriluk et al., 2016; Matias Santos et al., 2016; Jiang et al., 2019) may indeed be a systemic property in spiny mice that extends to critical internal organs as well. Similar to our transcriptome data, *Acomys* regeneration in skeletal muscle also demonstrated transcriptional activation of developmental pathways (Maden et al., 2018; Brant et al., 2019).

Our IPA analysis suggested that regulatory factors controlling cell cycle and DNA damage responses act to differentiate regenerative wound healing in *Acomys* from fibrogenic wound healing in *Mus*. Recent studies show that epigenetic factors can modulate nephron progenitor cell renewal and differentiation during development (Liu et al., 2018, 2020; Wanner et al., 2019). Furthermore, progression of acute kidney injury (AKI) and chronic kidney disease (CKD) can be modulated by epigenetic factors such as DNA methylation and histone modifications, some of which persist after AKI and likely promote fibrosis and CKD (Liu et al., 2017; Chawla et al., 2014; Ferenbach and Bonventre, 2015; Sharifian et al., 2018; Soofi et al., 2020). Recently, activating chromatin marks such as histone K4 trimethylation were shown to be dynamically regulated after kidney injury and play key roles in activating reparative programs such as *Sox9* expression in mice (Soofi et al., 2020). Our data suggest that the *Acomys* genome is poised to initiate scarless wound healing at the time of kidney injury. Whether and to what extent epigenetic pathways orchestrate this activation of poised genomic sites and set into motion pathways for scarless and regenerative wound healing pathways is an ongoing subject of investigation.

Our comparative transcriptomic analysis identified 843 genes in six unique gene clusters that are differentially regulated in the *Acomys* early cohort compared with *Mus*. Among these were cell-cycle control genes, particularly at the G2-M transition, DNA damage response and checkpoint regulation genes, S-phase entry genes, and cell survival genes. EdU labeling studies verified the increased cell-cycle progression and DNA synthesis in glomerular and epithelial cells, whereas, of particular interest, reduced cell proliferation was found in interstitial cells implicated in producing fibrotic tissue in mice and humans (Duffield, 2014; Humphreys, 2018; Kuppe et al., 2021). In addition, we found selective upregulation of nephrogenic genes including *Osr1*, *Ror1/2*, and *Cdh6*. Immunofluorescence and western blot studies verified the increased expression of *Cdh6* in expanding patches of tubular epithelial cells in *Acomys*. RNA scope *in situ* hybridization analysis showed co-expression of *Osr1* and *Cdh6* in the same cells within these expanding epithelial patches in *Acomys* but not *Mus*. Thus, the *Acomys* genome response to kidney injury included rapid activation of genes linked to cell-cycle progression, DNA damage response, developmental pathways, angiogenesis, and metabolism.

AKI initiates a fibrogenic cascade that leaves patients at high risk for developing CKD and progressive loss of renal function (Chawla et al., 2014; Ferenbach and Bonventre, 2015). Although elegant studies in *Mus* have produced substantial insights into the pathogenesis of renal fibrosis, translating these findings into therapeutic solutions has been disappointing. Wound healing in most adult mammals, including humans, is a process of repair that frequently replaces functional tissue, with a collagen-rich extracellular matrix resulting in maintenance of tissue integrity but often with a corresponding loss of organ function. By contrast, some fish and amphibian species can fully regenerate damaged tissue and restore organ function after amputation or severe tissue injuries without fibrosis (Kragl et al., 2009; Poss, 2010). In the zebrafish kidney, for example, there is evidence of formation of new nephrons after gentamicin nephrotoxicity (McC Campbell and Wingert, 2014). However, in adult mammals there are no reports of nephron formation *de novo* after kidney injury. We now provide evidence for a potentially transformative new mammalian model for kidney disease that has evolved a distinctly different wound healing response to kidney injury than the currently

studied mouse, rat, or human models. Whether spiny mice can completely restore kidney function after obstructive or ischemic injuries by forming new nephrons or by rapid and efficient repair of damaged nephrons with restoration of mature tissue structure is yet to be determined. In either case, our data suggest that an in-depth analysis of the molecular basis for scar-free regenerative wound healing in *Acomys* species could be a gateway for development of novel antifibrotic therapies for kidney disease.

Limitations of the study

The injury models we used, while common to the field, are biased toward endothelial and tubular injury and not specifically targeted to glomeruli or other elements of kidney function. In addition, we did not surgically resect kidney mass to address the question of complete *de novo* tissue regeneration, but experiments are currently planned to investigate this aspect of regeneration. Another limitation is that the gene expression studies were bulk RNA seq approaches that limit our understanding of how individual cell types respond to kidney injury. Although these methods have allowed us to identify a gene expression signature associated with kidney regeneration, more work is needed to delineate the functional mechanisms by which wound healing is redirected from fibrosis to regeneration in the spiny mouse kidney. Finally, because of the historical use of male mice in studies of kidney fibrosis with the injury models used, we only used male animals for these experiments.

STAR★METHODS

Detailed methods are provided in the online version of this paper and include the following:

- KEY RESOURCES TABLE
- RESOURCE AVAILABILITY
 - Lead contact
 - Materials availability
 - Data and code availability
- EXPERIMENTAL MODEL AND SUBJECT DETAILS
 - Animal husbandry
 - Experimental models
- METHOD DETAILS
 - Collagen content
 - Histological examination
 - F4/80 macrophage quantification
 - RNAScope *in situ* hybridization
 - Kidney function
 - Immunofluorescence
 - RNA sequencing analysis
 - Pathway analysis
 - Lightsheet ultramicroscopy
 - Thymidine pulse labeling
- QUANTIFICATION AND STATISTICAL ANALYSIS

SUPPLEMENTAL INFORMATION

Supplemental information can be found online at <https://doi.org/10.1016/j.isci.2021.103269>.

ACKNOWLEDGMENTS

This work was supported by a grant from the W.M. Keck Foundation; the US National Institutes of Health grants 1R01DK114149-01A1, 1R21OD-023838, and 5T32-DK007662; the Loie Power Robinson Stem Cell & Regenerative Medicine fund; and the Seattle Children's Research Institute. We thank Joseph V. Bonventre, Harvard Medical School, for helpful advice regarding acute kidney injury studies and Dr Andres Collazo, Caltech Biological Imaging Center, for assistance with light-sheet fluorescence imaging studies.

AUTHOR CONTRIBUTIONS

DMO, CMB, NB, KB, AT, XS, JO, AMP, and BRN performed the experiments. PW and KJM established and maintained breeding colony and IACUC protocols. DMO, DRB, and MWM designed the experiments. JWM, TKB, BRN, AET, EDN, and DMO performed the bioinformatics analysis for the transcriptome data.

DMO, CMB, and MWM wrote the manuscript. DMO, KJM, and MWM obtained funding for the project. All authors made critical input into editing the manuscript.

DECLARATION OF INTERESTS

The authors declare no competing interests.

Received: March 25, 2021

Revised: September 2, 2021

Accepted: October 12, 2021

Published: November 3, 2021

REFERENCES

- Adam, M., Potter, A.S., and Potter, S.S. (2017). Psychrophilic proteases dramatically reduce single cell RNA-seq artifacts: a molecular atlas of kidney development. *Development* 144, 3625–3632. <https://doi.org/10.1242/dev.151142>.
- Brant, J.O., Lopez, M.C., Baker, H.V., Barbazuk, W.B., and Maden, M. (2015). A comparative analysis of gene expression profiles during skin regeneration in mus and acomys. *PLoS One* 10, e0142931.
- Brant, J.O., Boatwright, J.L., Davenport, R., Sandoval, A.G.W., Maden, M., and Barbazuk, W.B. (2019). Comparative transcriptomic analysis of dermal wound healing reveals de novo skeletal muscle regeneration in *Acomys cahirinus*. *PLoS One* 14, e0216228. <https://doi.org/10.1371/journal.pone.0216228>.
- Chaabane, W., Pradauda, F., Buleon, M., Jaafar, A., Vallet, M., Rischmann, P., Galarreta, C.I., Chevalier, R.L., and Tack, I. (2013). Renal functional decline and glomerulotubular injury are arrested but not restored by release of unilateral ureteral obstruction (UUO). *Am. J. Physiol. Ren. Physiol.* 304, F432–F439. <https://doi.org/10.1152/ajprenal.00425.2012>.
- Chawla, L.S., Eggers, P.W., Star, R.A., and Kimmel, P.L. (2014). Acute kidney injury and chronic kidney disease as interconnected syndromes. *N. Engl. J. Med.* 371, 58–66. <https://doi.org/10.1056/NEJMra1214243>.
- Cho, E.A., Patterson, L.T., Brookhiser, W.T., Mah, S., Kintner, C., and Dressler, G.R. (1998). Differential expression and function of cadherin-6 during renal epithelium development. *Development* 125, 803–812.
- Clark, L.D., Clark, R.D., and Heber-Katz, E. (1998). A new murine model for mammalian wound repair and regeneration. *Clin. Immunol. Immunopathol.* 88, 35–45. <https://doi.org/10.1006/clim.1998.4519>.
- Dotd, H.U., Leischner, U., Schierloh, A., Jährling, N., Mauch, C.P., Deininger, K., Deussing, J.M., Eder, M., Ziegglängsberger, W., and Becker, K. (2007). Ultramicroscopy: three-dimensional visualization of neuronal networks in the whole mouse brain. *Nat. Methods* 4, 331–336. <https://doi.org/10.1038/nmeth1036>.
- Duffield, J.S. (2014). Cellular and molecular mechanisms in kidney fibrosis. *J. Clin. Invest.* 124, 2299–2306. <https://doi.org/10.1172/JCI72267>.
- Duffield, J.S., Lupher, M., Thannickal, V.J., and Wynn, T.A. (2013). Host responses in tissue repair and fibrosis. *Annu. Rev. Pathol.* 8, 241–276. <https://doi.org/10.1146/annurev-pathol-020712-163930>.
- Ferenbach, D.A., and Bonventre, J.V. (2015). Mechanisms of maladaptive repair after AKI leading to accelerated kidney aging and CKD. *Nat. Rev. Nephrol.* 11, 264–276. <https://doi.org/10.1038/nrneph.2015.3>.
- Gawriluk, T.R., Simkin, J., Thompson, K.L., Biswas, S.K., Clare-Salzler, Z., Kimani, J.M., Kiama, S.G., Smith, J.J., Ezenwa, V.O., and Seifert, A.W. (2016). Comparative analysis of ear-hole closure identifies epimorphic regeneration as a discrete trait in mammals. *Nat. Commun.* 7, 11164. <https://doi.org/10.1038/ncomms11164>.
- Grgic, I., Krautzberger, A.M., Hofmeister, A., Lalli, M., DiRocco, D.P., Fleig, S.V., Liu, J., Duffield, J.S., McMahon, A.P., Aronow, B., and Humphreys, B.D. (2014). Translational profiles of medullary myofibroblasts during kidney fibrosis. *J. Am. Soc. Nephrol.* 25, 1979–1990. <https://doi.org/10.1681/ASN.2013101143>.
- Gurtner, G.C., Werner, S., Brandon, Y., and Longaker, M.T. (2008). Wound repair and regeneration. *Nature* 453, 314–321. <https://doi.org/10.1038/nature07039>.
- Haddad, G., Kölling, M., Wegmann, U.A., Dettling, A., Seeger, H., Schmitt, R., Soerensen-Zender, I., Haller, H., Kistler, A.D., Dueck, A., et al. (2021). Renal AAV2-mediated overexpression of long non-coding RNA *H19* attenuates ischemic acute kidney injury through sponging of microRNA-30a-5p. *J. Am. Soc. Nephrol.* 32, 323–341. <https://doi.org/10.1681/ASN.2020060775>.
- Hendry, C., Rumballe, B., Moritz, K., and Little, M.H. (2011). Defining and redefining the nephron progenitor population. *Pediatr. Nephrol.* 26, 1395–1406. <https://doi.org/10.1007/s00467-010-1750-4>.
- Hill, N.R., Fatoba, S.T., Oke, J.L., Hirst, J.A., O'Callaghan, C.A., Lasserson, D.S., and Hobbs, F.D.R. (2016). Global prevalence of chronic kidney disease – a systematic review and meta-analysis. *PLoS One* 11, e0158765. <https://doi.org/10.1371/journal.pone.0158765>.
- Humphreys, B.D. (2018). Mechanisms of renal fibrosis. *Annu. Rev. Physiol.* 80, 309–326. <https://doi.org/10.1146/annurev-physiol-022516-034227>.
- Jiang, T.X., Harn, H.I.C., Ou, K.L., Lei, M., and Chuong, C.M. (2019). Comparative regenerative biology of spiny (*Acomys cahirinus*) and laboratory (*Mus musculus*) mouse skin. *Exp. Dermatol.* 28, 442–449. <https://doi.org/10.1111/exd.13899>.
- Keenan, A.B., Torre, D., Lachmann, A., Leong, A.K., Wojciechowski, M.L., Utti, V., Jagondik, K.M., Kropiwnick, i E., Wang, Z., and Ma'ayan, A. (2019). ChEA3: transcription factor enrichment analysis by orthogonal omics integration. *Nucleic Acids Res.* 47, W212–W224. <https://doi.org/10.1093/nar/gkz446>.
- Kragl, M., Knapp, D., Nacu, E., Khattak, S., Maden, M., Epperlein, H.H., and Tanaka, E.M. (2009). Cells keep a memory of their tissue origin during axolotl limb regeneration. *Nature* 460, 60–65. <https://doi.org/10.1038/nature08152>.
- Kuppe, C., Ibrahim, M.M., Kranz, J., Zhang, X., Ziegler, S., Perales-Patón, J., Jensen, J., Reimer, K.C., Smith, J.R., Dobie, R., et al. (2021). Decoding myofibroblast origins in human kidney fibrosis. *Nature* 589, 281–286. <https://doi.org/10.1038/s41586-020-2941-1>.
- Leischner, U., Schierloh, A., Ziegglängsberger, W., and Dotd, H.U. (2015). Formalin-induced fluorescence reveals cell shape and morphology in biological tissue samples. *PLoS One* 5, e010391. <https://doi.org/10.1371/journal.pone.0010391>.
- Liu, W., Li, X., Zhao, Y., Meng, X.M., Wan, C., Yang, B., Lan, H.Y., Lin, H.Y., and Xia, Y. (2013). Dragon (repulsive guidance molecule RGMb) inhibits E-cadherin expression and induces apoptosis in renal tubular epithelial cells. *J. Biol. Chem.* 288, 31528–31539. <https://doi.org/10.1074/jbc.M113.517573>.
- Liu, J., Kumar, S., Dolzhenko, E., Alvarado, G.F., Guo, J., Lu, C., Chen, Y., Li, M., Dessing, M.C., Parvez, R.K., et al. (2017). Molecular characterization of the transition from acute to chronic kidney injury following ischemia/reperfusion. *JCI Insight* 2, e94716. <https://doi.org/10.1172/jci.insight.94716>.
- Liu, H., Chen, S., Yao, X., Li, Y., Chen, C.H., Liu, J., Saifudeen, Z., and El-Dahr, S.S. (2018). Histone deacetylases 1 and 2 regulate the transcriptional programs of nephron progenitors and renal vesicles. *Development* 145, dev153619. <https://doi.org/10.1242/dev.153619>.
- Liu, H., Hilliard, S., Kelly, E., Chen, C.H., Saifudeen, Z., and El-Dahr, S.S. (2020). The polycomb proteins EZH1 and EZH2 co-regulate

- chromatin accessibility and nephron progenitor cell lifespan in mice. *J. Biol. Chem.* 295, 11542–11558. <https://doi.org/10.1074/jbc.RA120.013348>.
- Lund, S.P., Nettleton, D., McCarthy, D.J., and Smyth, G.K. (2012). Detecting differential expression in RNA-sequence data using quasi-likelihood with shrunken dispersion estimates. *Stat. Appl. Genet. Mol. Biol.* 11, 8. <https://doi.org/10.1515/1544-6115.1826>.
- Maden, M., Brant, J.O., Rubiano, A., Sandoval, A.G.W., Simmons, C., Mitchell, R., Collin-Hooper, H., Jacobson, J., Omairi, S., and Patel, K. (2018). Perfect chronic skeletal muscle regeneration in adult spiny mice, *Acomys cahirinus*. *Sci. Rep.* 8, 8920. <https://doi.org/10.1038/s41598-018-7>.
- Mah, S.P., Saueressig, M., Goulding, M., Kintner, C., and Dressler, G.R. (2000). Kidney development in cadherin-6 mutants: delayed mesenchyme-to-epithelial conversion and loss of nephrons. *Dev. Biol.* 223, 38–53. <https://doi.org/10.1006/dbio.2000.9738>.
- Mamrot, J., Legaie, R., Ellery, S.J., Wilson, T., Seeman, T., Powell, D.R., Gardner, D.K., Walker, D.W., Temple-Smith, P., Papenfuss, A.T., and Dickinson, H. (2017). De novo transcriptome assembly for the spiny mouse (*Acomys cahirinus*). *Sci. Rep.* 7, 8996. <https://doi.org/10.1038/s41598-017-09334-7>.
- Matias Santos, D., Rita, A.M., Casanellas, I., Brito Ova, A., Araujo, I.M., Power, D., and Tiscornia, G. (2016). Ear wound regeneration in the African spiny mouse *Acomys cahirinus*. *Regeneration* 3, 52–61. <https://doi.org/10.1002/reg2.50>.
- McCampbell, K.K., and Wingert, R.A. (2014). New tides: using zebrafish to study renal regeneration. *Transl. Res.* 163, 109–122. <https://doi.org/10.1016/j.trsl.2013.10.003>.
- O'Brien, L.L., and McMahon, A.P. (2011). Induction and patterning of the metanephric nephron. *Semin. Cell Dev. Biol.* 26, 1395–1406. <https://doi.org/10.1016/j.semcdb.2014.08.014>.
- Oh, Y.S., Thomson, L.E.J., Fishbein, M.C., Berman, D.S., Sharifi, B., and Chen, P.S. (2004). Scar formation after ischemic myocardial injury in MRL mice. *Cardiovasc. Pathol.* 13, 203–206. <https://doi.org/10.1016/j.carpath.2004.03.610>.
- Okamura, D.M., Pennathur, S., Pasichnyk, K., López-Guisa, J.M., Collins, S., Febbraio, M., Heinecke, J., and Eddy, A.A. (2009). CD36 regulates oxidative stress and inflammation in hypercholesterolemic CKD. *J. Am. Soc. Nephrol.* 20, 495–505. <https://doi.org/10.1681/ASN.2008010009>.
- Okamura, D.M., Bahrami, N.M., Ren, S., Pasichnyk, K., Williams, J.M., Gangotri, J.A., López-Guisa, J.M., Yamaguchi, I., Barshop, B.A., Duffield, J.S., and Eddy, A.A. (2014). Cysteamine modulates oxidative stress and blocks myofibroblast activity in CKD. *J. Am. Soc. Nephrol.* 25, 43–54. <https://doi.org/10.1681/ASN.2012090962>.
- Oxburgh, L. (2018). Kidney nephron determination. *Annu. Rev. Cell Dev. Biol.* 34, 427–450. <https://doi.org/10.1146/annurev-cellbio-100616-060647>.
- Pennathur, S., Pasichnyk, K., Bahrami, N.M., Zeng, L., Febbraio, M., Yamaguchi, I., and Okamura, D.M. (2015). The macrophage phagocytic receptor CD36 promotes fibrogenic pathways on removal of apoptotic cells during chronic kidney disease. *Am. J. Pathol.* 185, 2232–2245. <https://doi.org/10.1016/j.ajpath.2015.04.016>.
- Poss, K.D. (2010). Advances in understanding tissue regenerative capacity and mechanisms in animals. *Nat. Rev. Genet.* 11, 710–722. <https://doi.org/10.1038/nrg2879>.
- Renier, N., Wu, Z., Simon, D.J., Yang, J., Ariel, P., and Tessier-Lavigne, M. (2014). iDISCO: a simple, rapid method to immunolabel large tissue samples for volume imaging. *Cell* 159, 896–910. <https://doi.org/10.1016/j.cell.2014.10.010>.
- Robey, T.E., and Murry, C.E. (2008). Absence of regeneration in the MRL/MpJ mouse heart following infarction or cryoinjury. *Cardiovasc. Pathol.* 17, 6–13. <https://doi.org/10.1016/j.carpath.2007.01.005>.
- Robinson, M.D., McCarthy, D.J., and Smyth, G.K. (2010). edgeR: a Bioconductor package for differential expression analysis of digital gene expression data. *Bioinformatics* 26, 139–140. <https://doi.org/10.1093/bioinformatics/btp616>.
- Rockey, D.C., Bell, P.D., and Hill, J.A. (2015). Fibrosis: a common pathway to organ injury and failure. *N. Engl. J. Med.* 372, 1138–1149. <https://doi.org/10.1056/NEJMra1300575>.
- Seifert, A.W., Kiama, S.G., Seifert, M.G., Goheen, J.R., Palmer, T.M., and Maden, M. (2012). Skin shedding and tissue regeneration in African spiny mice (*Acomys*). *Nature* 489, 561–565. <https://doi.org/10.1038/nature11499>.
- Sharifian, R., Okamura, D.A., Denisenko, O., Zager, R.A., Johnson, A., Gharib, S.A., and Bomsztyk, K. (2018). Distinct patterns of transcriptional and epigenetic alterations characterize acute and chronic kidney injury. *Sci. Rep.* 8, 17870. <https://doi.org/10.1038/s41598-018-35943-x>.
- Simkin, J., Gawriluk, T.R., Gensel, J.C., and Seifert, A.W. (2017). Macrophages are necessary for epimorphic regeneration in African spiny mice. *eLife* 6, e24623. <https://doi.org/10.7554/eLife.24623>.
- Soofi, A., Kutschat, A.P., Azam, M., Laszczyk, A.M., and Dressler, G.R. (2020). Regeneration after acute kidney injury requires PTIP-mediated epigenetic modifications. *JCI Insight* 5, 1–13. <https://doi.org/10.1172/jci.insight.130204>.
- Tapmeier, T.T., Brown, K.L., Tang, Z., Sacks, S.H., Sheerin, N.S., and Wong, W. (2008). Reimplantation of the ureter after unilateral ureteral obstruction provides a model that allows functional evaluation. *Kidney Int.* 73, 885–889. <https://doi.org/10.1038/sj.ki.5002797>.
- Wanner, N., Vornweg, J., Combes, A., Wilson, S., Plappert, J., Rafflenbeul, G., Puelles, V.G., Rahman, R.U., Liwinski, T., Lindner, S., et al. (2019). DNA methyltransferase 1 controls nephron progenitor cell renewal and differentiation. *J. Am. Soc. Nephrol.* 30, 63–78. <https://doi.org/10.1681/ASN.2018070736>.
- Yermalovich, A.V., Osborne, J.K., Sousa, P., Han, A., Kinney, M.A., Chen, M.J., Robinton, D.A., Montie, H., Pearson, D.S., Wilson, S.B., et al. (2019). Lin28 and let-7 regulate the timing of cessation of murine nephrogenesis. *Nat. Commun.* 10, 168. <https://doi.org/10.1038/s41467-018-08127-4>.
- Zheng, G., Zhang, J., Zhao, H., Wang, H., Pang, M., Qiao, X., Lee, S.R., Hsu, T.T., Tan, T.K., Lyons, J.G., et al. (2016). $\alpha 3$ Integrin of cell-cell contact mediates kidney fibrosis by integrin-linked kinase in proximal tubular E-cadherin deficient mice. *Am. J. Pathol.* 186, 1847–1860. <https://doi.org/10.1016/j.ajpath.2016.03.015>.

STAR★METHODS

KEY RESOURCES TABLE

REAGENT or RESOURCE	SOURCE	IDENTIFIER
Antibodies		
Mouse monoclonal anti-Actin, alpha Smooth Muscle (clone 1A4) (Acta2)	Sigma-Aldrich	Cat# A2547; RRID: AB_476701
Rabbit polyclonal pan-Laminin	Abcam	Cat# ab11575; RRID: AB_298179
Rat monoclonal F4/80	Thermo Fisher Scientific	Cat# MF48000; RRID: AB_10376289
Mouse monoclonal E cadherin (Cdh1)	BD Biosciences	Cat# 610181; RRID: AB_397581
Rabbit monoclonal ZO-1	Abcam	Cat# ab221547; RRID: AB_2892660
Mouse monoclonal anti-Vinculin	Sigma-Aldrich	Cat# V9131; RRID: AB_477629
Donkey polyclonal anti-Rabbit IgG (H+L), 488	Jackson ImmunoResearch	Cat# 711-545-152; RRID: AB_2313584
Donkey polyclonal anti-Rabbit IgG (H+L), 594	Jackson ImmunoResearch	Cat# 711-585-152; RRID: AB_2340621
Donkey polyclonal anti-Rat IgG (H+L), Cy3	Jackson ImmunoResearch	Cat# 712-165-153; RRID: AB_2340667
Donkey polyclonal anti-Rat (H+L), HRP	ThermoFisher	Cat# A18739; RRID: AB_2535516
Goat polyclonal anti-Rabbit IgG (H+L), HRP	Jackson ImmunoResearch	Cat# 111-035-003; RRID: AB_2313567
Goat polyclonal anti-Rat (H+L), Cross adsorbed Cy3	ThermoFisher	Cat# A10522; RRID: AB_2534031
Goat polyclonal anti-Mouse IgG1 Secondary Antibody, Alexa Fluor 488 conjugate	Thermo Fisher Scientific	Cat# A-21121; RRID: AB_2535764
Goat polyclonal anti-Mouse IgG2a Cross-Adsorbed Secondary Antibody, Alexa Fluor 488	Thermo Fisher Scientific	Cat# A-21131; RRID: AB_2535771
Goat polyclonal anti-Mouse IgG2a Cross-Adsorbed Secondary Antibody, Alexa Fluor 594	Thermo Fisher Scientific	Cat# A-21135; RRID: AB_2535774
Goat polyclonal anti-Rabbit IgG (H+L) Cross-Adsorbed Secondary Antibody, Alexa Fluor 488	Thermo Fisher Scientific	Cat# A-11008; RRID: AB_143165
Goat polyclonal anti-Rabbit IgG (H+L) Cross-Adsorbed Secondary Antibody, Alexa Fluor 594	Thermo Fisher Scientific	Cat# A-11012; RRID: AB_2534079
IRDye® 680RD Goat anti-Mouse IgG (H+L)	LI-COR Biosciences	Cat# 925-68070; RRID: AB_2651128
IRDye® 800CW Goat anti-Rabbit IgG (H+L)	LI-COR Biosciences	Cat# 925-32211; RRID: AB_2651127
Chemicals, peptides, and recombinant proteins		
Normal Donkey serum	Jackson ImmunoResearch	Cat# 017-000-001; RRID: AB_2337254
Normal Goat serum	Jackson ImmunoResearch	Cat# 005-000-121; RRID: AB_2336990
Alexa Fluor 555 Tyramide Reagent	ThermoFisher	Cat# B40955
Alexa Fluor 488 Tyramide Reagent	ThermoFisher	Cat# B40953
Critical commercial assays		
RNAScope Multiplex Fluorescent V2 Mus and custom <i>Acomys cahirinus</i> RNA probes	ACD Bio	custom
Urea nitrogen (BUN) colorimetric detection kit	Arbor Assays	Cat#: K024-H1
Mouse creatinine assay kit	Crystal Chem	Cat#: 80350
Deposited data		
UUO <i>Acomys</i> and Mus RNA Seq transcriptome	GEO	GSE168876
Experimental models: Organisms/strains		
<i>Acomys cahirinus</i> : African Spiny Mouse	This study	N/A
<i>Mus musculus</i> : Crl:CD1(ICR)	Charles River	RRID: IMSR_CRL:22
<i>Mus musculus</i> : C57BL6/J	Jackson	RRID: IMSR_CRL:22

(Continued on next page)

Continued

REAGENT or RESOURCE	SOURCE	IDENTIFIER
Software and algorithms		
Fiji (Image J)	http://fiji.sc/	N/A
Image Pro v7	Media Cybernetics	N/A
Imaris 7.4	Bitplane	N/A
Image Studio Light V5.2	https://www.licor.com/bio	N/A
VS-Desktop	Olympus	N/A
Prism7.03	Graph Pad	N/A
Stata14	StataCorp	N/A
EdgeR	https://bioconductor.org/packages/release/bioc/html/edgeR.html	N/A
Ingenuity Pathway Analysis	Qiagen	N/A
ChIP-X Enrichment Analysis V3	https://maayanlab.cloud/chea3/	N/A
Other		
Leica TCS SP5 Confocal LSM	Leica	N/A
Leica DM4000B microscope	Leica	N/A
BD Biosciences LSR II Flow Cytometer	BD Biosciences	N/A

RESOURCE AVAILABILITY**Lead contact**

Further information and reasonable requests for resources and reagents should be directed to and will be fulfilled by the lead contact Dr. Mark W. Majesky (mwm84@uw.edu).

Materials availability

Materials used in this study are available from the lead contact upon reasonable request.

Data and code availability

- RNA-seq data presented in [Figure 3](#) have been deposited at GEO and are publicly available at #GSE168876.
- This paper does not report original code.
- Any additional information required to reanalyze the data reported in this paper is available from the lead contact upon request.

EXPERIMENTAL MODEL AND SUBJECT DETAILS**Animal husbandry**

The Seattle Children's Research Institute's (SCRI) Institutional Animal Care and Use Committee (IACUC) approved all animal procedures. Adult male *Mus musculus* (C57BL/6J (B6), CD-1 – source - The Jackson Laboratory) and *Acomys cahirinus* (colony at SCRI) were maintained within the Seattle Children's Research Institute's onsite vivarium. B6 and CD1 mice were housed in a pathogen-free room maintained on 12:12 (Light:Dark) lighting schedule, *Acomys* were housed in a separate room maintained on 14:10 (Light:Dark) schedule, and all animals received food and water ad libitum.

Experimental models

We utilized two models of kidney injury to investigate the differences in wound healing and fibrosis: Unilateral ureteral obstruction (UUO) and ischemia reperfusion injury (IRI). B6 and CD-1 mice were used as inbred and outbred strains of *Mus*, respectively. Surgery was performed on male animals between 3 and 6 months of age, male littermates were randomly assigned to experimental groups. UUO surgeries were performed ([Okamura et al., 2009, 2014](#)) (n = 6–8/group), and animals were sacrificed at 3, 7, 14,

and 21 days after surgery. Mice received isoflurane anesthesia (5% induction; 1-3% maintenance) in oxygen through a precision vaporizer (Portable Anesthesia Machine, PAM; Molecular Imaging Products, Bend, OR, USA). Acomys received isoflurane anesthesia at 3-4% due to some sensitivity to larger doses of isoflurane. The incision site was shaved and sterile prepped with Betadine and ethanol. A 0.5 cm anterior vertical incision was made in the left lower quadrant. The left ureter was identified and tied with two 4-0 silk sutures placed close to the pelvis of the kidney. Sham animals had their ureter manipulated without placement of silk suture. Warmed saline was given intraperitoneal. The muscle layer was closed with 4-0 Webcryl absorbable sutures (Patterson Veterinary Supply, #V397) and the skin was closed with 4-0 Weblon nylon sutures (Patterson Veterinary Supply, #662BL). Animals received buprenorphine (Patterson Veterinary Supply, #07-892-5235) 0.1 mg/kg perioperatively and postoperatively per IACUC guidelines for pain control.

Unilateral IRI (uni-IRI) surgeries were performed (Okamura et al., 2014; Pennathur et al., 2015) and that the vascular pedicle was clamped for 40 minutes (n = 5–6/group), and animals were sacrificed at 24 h, 72 h, 7 days, and 14 days after surgery. Animals received isoflurane induction as noted above. The incision site was shaved and sterile prepped with Betadine and ethanol. Animals were kept at a constant temperature (37°C) with TCAT-2 temperature controller (Braintree Scientific, #TCAT2DF) during the entire procedure. A 1 cm anterior horizontal incision was made in the mid right quadrant. The left renal vascular pedicle was identified and a vascular clamp (Braintree Scientific, #MVC02) was placed for 40 minutes, with confirmation of ischemia and reperfusion. Sham animals had their vascular pedicle manipulated without placement of clamp. Warmed saline was given intraperitoneal. The muscle layer was closed with 4-0 Webcryl absorbable sutures (Patterson Veterinary Supply, #V397) and the skin was closed with 4-0 Weblon nylon sutures (Patterson Veterinary Supply, #662BL). Animals received buprenorphine (Patterson Veterinary Supply, #07-892-5235) 0.1 mg/kg perioperatively and postoperatively per IACUC guidelines for pain control. In select cases, in order to assess initial injury, the contralateral kidney was removed at the time of uni-IRI surgery and sacrificed at 24 h after surgery. In select cases, in order to quantify kidney function in the uni-IRI kidney after initial injury, a contralateral nephrectomy was performed 14 days post-surgery (Okamura et al., 2014). Blood was drawn daily until sacrifice at 2 days post-nephrectomy. All procedures were performed in accordance with the guidelines established by National Research Council Guide for the Care and Use of Laboratory Animals and approval of our Institute Animal Care and Use Committee (IACUC). Contralateral, UUC, and IRI kidneys were harvested and processed for RNA and protein extraction and histological studies (Okamura et al., 2014; Pennathur et al., 2015). Frozen tissue samples were stored at -80°C.

METHOD DETAILS

Collagen content

Hydroxyproline content of kidney tissue (μg of hydroxyproline per mg of wet weight kidney section) was measured by acid hydrolysis of the tissue section (Okamura et al., 2009, 2014). Frozen kidney tissue was weighed and placed in a 16 mm glass tube with sealed cap with 500 μl 12N HCl. Samples were boiled in a heating block for 2-3 minutes at 100°C and vortex intermittently to dissolve tissue completely. Temperature was increased to 110°C for acid hydrolysis of proteins overnight in hood. Caps were screwed on tightly. Temperature was decreased to 75°C and caps opened to allow sample to dry thoroughly overnight. Dried samples were solubilized in 500 μl of Collagen buffer (Citric acid, pH 6.1). Vortex and pipette to mix. Particulates were removed with a 0.45 μm centrifugal filter unit (Ultrafree MC Millipore #UFC30HVNB). Chloramine T solution and DMB solution were made on the day of assay. Samples were heated to 65°C. Collagen (hydroxyproline) standards (100 ng, 200 ng, 500 ng, 1000 ng, and 2000 ng) were used, 10 μl of sample was placed in a 96 well microtiter plate and 100 μl of fresh Chloramine T solution was added to start oxidation reaction. Plate was kept at room temperature for 15 minutes, then 100 μl of fresh DMB was added. Samples were placed at 65°C for 20 minutes. Reaction was stopped by placing on ice for 3 minutes. Samples were read on a microtiter plate reader at 550 nm. Conversion factor for ng of hydroxyproline in sample of total collagen is 7.83.

Histological examination

Immunohistochemical staining was performed on sections of paraffin-embedded tissue or cryosections of snap-frozen tissue using procedures established in our laboratory with VECTASTAIN *Elite* ABC Kits (Vector Laboratories, Inc.) and AEC Substrate Chromogen K3464 (Dako Corp.). Sections were blocked with Avidin/Biotin blocking kit (Vector Laboratories, Inc.). Computer-assisted image analysis was performed on 6 randomly selected 400x magnified images of slides from individual animals with Image-Pro Plus software (Mediatech). The investigator was blinded to the experimental groups at the time of analysis. Picrosirius

red staining was performed (Okamura et al., 2014; Pennathur et al., 2015). Paraffin slides were rehydrated. Slides were stained with 0.1% picosirius red for one hour at room temperature and washed in two changes of acidified water. Slides were dehydrated and mounted with VectaMount permanent mounting medium. Quantification of interstitial staining of picosirius red (SR) staining was performed in a blinded manner using Image-Pro/ImageJ software with randomly selected cortical fields. SR glomerular staining was subtracted and net SR area was normalized to net tubulointerstitial area of 400x field (Net area = Total – glomerular area - empty space). Masson Trichrome and hematoxylin eosin stains were performed on paraffin sections by standard protocols. Interstitial fibrosis and tubular atrophy (IFTA) scores were analyzed on 6 randomly selected 400x Masson Trichrome stained images. The following IFTA scores were assigned, in a blinded manner, based on the estimated percent area affected with tubular atrophy, loss of tubular structure, interstitial inflammation, and interstitial fibrosis in the field: 1 (normal); 2 (<10%), 3 (10-25%); 4 (26-50%); or 5 (>50%). Dilated tubular area was measured using Image-Pro software on 400x Masson trichrome stained images. Tubular casts and intraluminal debris area was measured using Image-Pro software on 200x PAS-stained images and normalized to net tubulointerstitial area for 6 randomly selected cortical fields. Secondary antibodies were shown to be non-reactive with tissue sections stained without the primary antibody.

F4/80 macrophage quantification

Animals were perfused with cold normal saline and contralateral and UUO kidneys were placed on ice, minced, digested with Liberase TL (Roche) with 1% DNase (Sigma-Aldrich), then placed at 37°C for 10 minutes and vortexed intermittently. An equal volume of ice-cold HBSS+10%FBS was added to stop Liberase/DNase. Glomeruli were removed by passing cell suspension through a 40 µm Nylon filter. Cells were stained per protocol with DAPI, PE-Cy7-anti-CD45, PE-anti-CD11b, APC-eFluor780-F4/80 from BD Biosciences. Cells were blocked with mouse Fc Block (BD Biosciences). Leukocytes were identified and gated based on their positive F4/80 expression. Data was acquired on the LSR II flow cytometer (BD Biosciences) and analyzed using FlowJo software (Tree Star, Inc).

RNAScope *in situ* hybridization

RNAScope was performed on B6 and *Acomys* kidney tissue by ACD Bio-Techne. Unique multiplex fluorophore control (*Polr2a*, *Ppib*, *Ubc*, *Hprt*) and target (*Cdh6*, *Osr1*) probes for both *Mus* and *Acomys* were designed by Advanced Cell Diagnostics (ACDBio). Freshly cut cryosections from day 3 IRI tissue were sent and sample quality control and optimization was performed by ACDBio on kidney tissue. Multiplex RNAScope was performed on cryosections from individual animals (n = 3/group) with both control and target probes at ACDBio and returned to our lab. Samples were imaged on a Leica SP5 confocal microscope (six 400x images/slide). Image analysis was performed on *Cdh6* and *Osr1* and analyzed by GraphPad Prism.

Kidney function

Serum was analyzed for blood urea nitrogen (BUN) using the Urea Nitrogen (BUN) Reagent Set kit (Arbor Assays). Serum was analyzed for creatinine content using the Mouse Creatinine Kit, Enzymatic (Crystal Chem, Inc.). Samples were processed according to manufacturer's protocol. All samples were performed in triplicate.

Immunofluorescence

For cryosectioning, excised tissue was embedded and flash-frozen in O.C.T medium (Tissue Tech) using a dry-ice slurry/2-methylbutanol mixture and cryosectioned between 8-10µm. Tissue cryosections were washed with PBS and fixed with 4% PFA for 10 min. Post fixation, slides were washed three times for 5 min each with PBS followed by permeabilization using 0.2% Triton-X100 in PBS (PBT) for 10 min. Slides were then blocked (5% BSA, 2% normal goat serum in PBT) at room temperature for 1hr. Post block, tissue sections were then incubated in primary antibody overnight at 4°C in blocking solution (3% BSA, 0.2% Triton-X100 in PBS). Primary antibodies used include pan-Laminin (Abcam, #ab11575), *Acta2* (Sigma, #A2547), F4/80 (Invitrogen, #MF48000), *Cdh1* (BD Bioscience, #610181), and ZO-1/Tjp1 (Abcam, #ab221547). After overnight incubation, slides were washed with PBS, and then incubated with goat ALEXA-Fluor 594- or ALEXA-Fluor 488- conjugated antibodies (Thermo Fisher Scientific) for 2 h at room temperature in blocking solution. Cell nuclei were counterstained with DAPI (Molecular Probes) and mounted in 4% (w/v) propyl gallate anti-fade solution. Immunofluorescent images were obtained using

an SP5 confocal microscope (Leica). *Acta2* and *Cdh1* confocal image quantification analysis was performed as noted above (Okamura et al., 2014; Pennathur et al., 2015).

RNA sequencing analysis

Age-matched adult male C57BL/6J (B6) and *Acomys* (2-4 months) were subjected to unilateral ureter obstruction (UUO) procedure at the left ureter. Kidneys from sham operated controls and UUO-treated animals after 2 and 5 days were collected after perfusion with ice-cold normal saline and flash frozen in liquid nitrogen. Total RNA was extracted from kidney using Trizol (Invitrogen) and Direct-zol RNA Kit (R2072, Zymo Research) according to manufacturer instructions. RNA samples were analyzed with Agilent 6000 RNA Nano Kit at Bioanalyzer 2100 for quality assurance and then submitted to Novogene (Chula Vista, CA) for oligo-dT based mRNA enrichment, cDNA library generation with random hexamers, and Illumina sequencing at 50M reads in paired end 100bp sequencing conditions. The *Acomys* transcript data was aligned to the Tr2aacds transcriptome (19), and re-annotated by blasting against the mouse transcriptome. We obtained an average of 57 million reads from both *Mus* and *Acomys* libraries, mapped >75% of reads to a transcript in mouse transcriptome and *Acomys* Tr2aacds transcriptome for homology-based identification (Table S3).

Bioconductor edgeR package was used to filter out genes with consistently low levels of expression, and to linear model, fit and count data (Robinson et al., 2010). We made comparisons between within-species groups using quasi-likelihood F-tests at a log fold change of 0.585, which is equal to a linear fold change of 1.5, or a 50% difference in expression between groups, and a false discovery rate (FDR) of 0.05 (Lund et al., 2012). This approach generated approximately 3900-5300 *Mus* and approximately 1700-2500 *Acomys* differentially expressed transcripts between UUO injured and sham operated control kidneys in the same species. Genes with conserved increased or decreased differential expression profiles between injured and sham operated kidneys were identified. Non-conserved species-specific gene expression differences were also identified by using limma voom function to fit data to a linear model, first considering within species differences between time points to obviate potential technical differences between transcriptome assemblies and completeness, followed by empirical Bayes adjusted interaction tests for the d2 vs sham, d5 vs sham and d5 vs d2 comparisons, such as (d2*Acomys* – sham*Acomys*) – (d2*Mus* – sham*Mus*). This resulted in identification of approximately 500-800 statistically significant transcript interactions between species that exhibited a non-conserved change in expression level at an FDR < 0.05 and a 1.5 linear fold change (logFC > 0.585) within one of the 4 groups. To visualize interaction data, we averaged the expression level for a given gene across each comparison, calculated the difference from the mean, and color-coded gene z-scores to reflect the magnitude of expression differences.

Pathway analysis

Ingenuity Pathway Analysis (version 01-19-02, QIAGEN) was used to identify the most significant canonical pathways based on differentially expressed transcripts between UUO and sham as determined by RNA sequencing, using linear fold change of expression -2 to +2 and FDR>0.05 as cutoffs for the analysis. Here we increased the absolute fold change from 1.5 to 2 in order to more stringently identify important pathways. The top 15 most significant differentially regulated canonical pathways by *p*-value for B6 and *Acomys* are reported along with the activation z-score. The z-score was calculated by IPA and was based on the direction of effect of each differentially regulated gene within a pathway and predicted whether a pathway was up or down regulated after day 2 UUO. Transcription factor enrichment analysis was performed using ChIP-X Enrichment Analysis Version 3 (ChEA3), which applied the Fisher's Exact Test to compare genes from clusters 2 and 3 of the RNA sequencing analysis to transcription factor – target interactions from published ChIP-Seq and co-expression databases (Keenan et al., 2019).

Lightsheet ultramicroscopy

B6 and *Acomys* UUO and IRI and contralateral control kidneys were collected from animals after 14 days of injury. Animals were perfused with PBS and then 4% PFA-PBS solution, kidneys were removed and post-fixed in 4%PFA overnight at 4°C. Kidneys were dehydrated through a methanol series, delipidated, and cleared using the iDISCO protocol (Renier et al., 2014). Cleared kidneys were imaged with an UltraMicroscope (LaVision Biotech), using 488 nm lightsheet with a Z-step of 3 μm, across multiple magnifications (μm to mm). Image volumes were assembled and analyzed using Imaris (Bitplane) and FIJI. Cortex region of interest (ROI) was manually defined (kidney outer surface to cortex/medulla boundary) using Surfaces. High-

contrast regions within the cortex ROI were automatically/semi-automatically rendered and segmented using Surfaces in Imaris.

Thymidine pulse labeling

Age-matched adult male C57BL/6J (B6) and *Acomys* (2-4 months) normal/uninjured ($n = 4$) and uni-IRI ($n = 6$) received EdU (50 mg/kg) intraperitoneally starting on the day of surgery and every 2 days until sacrifice at day 14. Cryosections were stained using the Click-IT kit 594 (ThermoFisher) along with Cdh1 and ZO-1/Tjp1, imaged by confocal microscopy. Digital images were obtained and image analysis performed on six images per animal.

QUANTIFICATION AND STATISTICAL ANALYSIS

All data are presented as the mean and standard error. All statistical analyses were performed using GraphPad PRISM 7.0 (GraphPad Software) and STATA 14 (StataCorp LP) software. Two-way analysis of variance (ANOVA) was performed for all parametric data including computer-assisted image analysis data for time and species. For image analysis data, the arithmetic mean of six randomly selected images of slides for each animal was used for the two-way ANOVA. Sidak's and Tukey's multiple comparison post-tests were utilized for time and species, respectively. Nonparametric data (IFTA and tubular injury scores) were analyzed using the Mann-Whitney U test. A p value < 0.05 was considered statistically significant. UO kidney weights were analyzed by linear regression.